



MINISTÉRIO DA CIÊNCIA, TECNOLOGIA E INOVAÇÕES
INSTITUTO NACIONAL DE PESQUISAS ESPACIAIS

sid.inpe.br/mtc-m21d/2022/03.30.21.34-TDI

SEARCH FOR GRAVITATIONAL-WAVE BURSTS IN THE LIGO DATA AT THE SCHENBERG SENSITIVITY RANGE

Julio César Martins

Master's Dissertation of the Graduate Course in Astrophysics, guided by Drs. Odylio Denys de Aguiar, Ik Siong Heng, and Iara Tosta e Melo, approved in March 28, 2022.

URL of the original document:

<<http://urlib.net/8JMKD3MGP3W34T/46KAJQH>>

INPE
São José dos Campos
2022

PUBLISHED BY:

Instituto Nacional de Pesquisas Espaciais - INPE
Coordenação de Ensino, Pesquisa e Extensão (COEPE)
Divisão de Biblioteca (DIBIB)
CEP 12.227-010
São José dos Campos - SP - Brasil
Tel.:(012) 3208-6923/7348
E-mail: pubtc@inpe.br

**BOARD OF PUBLISHING AND PRESERVATION OF INPE
INTELLECTUAL PRODUCTION - CEPPII (PORTARIA Nº
176/2018/SEI-INPE):****Chairperson:**

Dra. Marley Cavalcante de Lima Moscati - Coordenação-Geral de Ciências da Terra
(CGCT)

Members:

Dra. Ieda Del Arco Sanches - Conselho de Pós-Graduação (CPG)
Dr. Evandro Marconi Rocco - Coordenação-Geral de Engenharia, Tecnologia e
Ciência Espaciais (CGCE)
Dr. Rafael Duarte Coelho dos Santos - Coordenação-Geral de Infraestrutura e
Pesquisas Aplicadas (CGIP)
Simone Angélica Del Ducca Barbedo - Divisão de Biblioteca (DIBIB)

DIGITAL LIBRARY:

Dr. Gerald Jean Francis Banon
Clayton Martins Pereira - Divisão de Biblioteca (DIBIB)

DOCUMENT REVIEW:

Simone Angélica Del Ducca Barbedo - Divisão de Biblioteca (DIBIB)
André Luis Dias Fernandes - Divisão de Biblioteca (DIBIB)

ELECTRONIC EDITING:

Ivone Martins - Divisão de Biblioteca (DIBIB)
André Luis Dias Fernandes - Divisão de Biblioteca (DIBIB)



MINISTÉRIO DA CIÊNCIA, TECNOLOGIA E INOVAÇÕES
INSTITUTO NACIONAL DE PESQUISAS ESPACIAIS

sid.inpe.br/mtc-m21d/2022/03.30.21.34-TDI

SEARCH FOR GRAVITATIONAL-WAVE BURSTS IN THE LIGO DATA AT THE SCHENBERG SENSITIVITY RANGE

Julio César Martins

Master's Dissertation of the Graduate Course in Astrophysics, guided by Drs. Odylio Denys de Aguiar, Ik Siong Heng, and Iara Tosta e Melo, approved in March 28, 2022.

URL of the original document:

<<http://urlib.net/8JMKD3MGP3W34T/46KAJQH>>

INPE
São José dos Campos
2022

Cataloging in Publication Data

Martins, Julio César.

M366s Search for gravitational-wave bursts in the ligo data at the schenberg sensitivity range / Julio César Martins. – São José dos Campos : INPE, 2022.

xx + 86 p. ; (sid.inpe.br/mtc-m21d/2022/03.30.21.34-TDI)

Dissertation (Master in Astrophysics) – Instituto Nacional de Pesquisas Espaciais, São José dos Campos, 2022.

Guiding : Drs. Odylio Denys de Aguiar, Ik Siong Heng, and Iara Tosta e Melo.

1. Gravitational wave. 2. Data analysis. 3. LIGO. 4. Coherent WaveBurst. 5. Schenberg. I.Title.

CDU 551.511.31:52



Esta obra foi licenciada sob uma Licença [Creative Commons Atribuição-NãoComercial 3.0 Não Adaptada](https://creativecommons.org/licenses/by-nc/3.0/).

This work is licensed under a [Creative Commons Attribution-NonCommercial 3.0 Unported License](https://creativecommons.org/licenses/by-nc/3.0/).



MINISTÉRIO DA
CIÊNCIA, TECNOLOGIA
E INOVAÇÕES



INSTITUTO NACIONAL DE PESQUISAS ESPACIAIS
Serviço de Pós-Graduação - SEPGR

DEFESA FINAL DE DISSERTAÇÃO DE JULIO CÉSAR MARTINS
BANCA Nº 049/2022, REG 857850/2020

No dia 28 de março de 2022, às 09h, por teleconferência, o(a) aluno(a) mencionado(a) acima defendeu seu trabalho final (apresentação oral seguida de arguição) perante uma Banca Examinadora, cujos membros estão listados abaixo. O(A) aluno(a) foi APROVADO(A) pela Banca Examinadora, por unanimidade, em cumprimento ao requisito exigido para obtenção do Título de Mestre em Astrofísica. O trabalho precisa da incorporação das correções sugeridas pela Banca Examinadora e revisão final pelo(s) orientador(es).

Título: "SEARCH FOR GRAVITATIONAL-WAVE BURSTS IN THE LIGO DATA AT THE SCHENBERG SENSITIVITY RANGE"

Membros da banca:

Dr. José Carlos Neves de Araujo - Presidente- INPE

Dr. Odylio Denys de Aguiar - Orientador - INPE

Dr. Ik Siong Heng - Orientador - University of Glasgow/SUPA

Dra. Iara Tosta e Melo - Orientadora - INFN/LNS

Dr. Rafael da Costa Nunes - Membro Interno - INPE

Dr. Rubens de Melo Marinho Junior - Membro Externo - Aposentado/ITA/IEF

Declaração de aprovação do Dr. Ik Siong Heng anexa ao processo.



Documento assinado eletronicamente por **Odylio Denys de Aguiar, Pesquisador**, em 29/03/2022, às 14:15 (horário oficial de Brasília), com fundamento no § 3º do art. 4º do [Decreto nº 10.543, de 13 de novembro de 2020](#).



Documento assinado eletronicamente por **José Carlos Neves de Araújo, Pesquisador**, em 29/03/2022, às 14:25 (horário oficial de Brasília), com fundamento no § 3º do art. 4º do [Decreto nº 10.543, de 13 de novembro de 2020](#).



Documento assinado eletronicamente por **Rafael da Costa Nunes (E), Usuário Externo**, em 29/03/2022, às 15:35 (horário oficial de Brasília), com fundamento no § 3º do art. 4º do [Decreto nº 10.543, de 13 de novembro de 2020](#).



Documento assinado eletronicamente por **Iara Tosta e Melo (E), Usuário Externo**, em 30/03/2022, às 05:18 (horário oficial de Brasília), com fundamento no § 3º do art. 4º do [Decreto nº 10.543, de 13 de novembro de 2020](#).



Documento assinado eletronicamente por **RUBENS DE MELO MARINHO JUNIOR (E)**, Usuário **Externo**, em 31/03/2022, às 10:01 (horário oficial de Brasília), com fundamento no § 3º do art. 4º do [Decreto nº 10.543, de 13 de novembro de 2020](#).



A autenticidade deste documento pode ser conferida no site <http://sei.mctic.gov.br/verifica.html>, informando o código verificador **9620285** e o código CRC **9B9FBC5D**.

Referência: Processo nº 01340.001572/2022-31

SEI nº 9620285

“Science is far from a perfect instrument of knowledge. It’s just the best we have. In this respect, as in many others, it’s like democracy. Science by itself cannot advocate courses of human action, but it can certainly illuminate the possible consequences of alternative courses of action”.

CARL SAGAN

in *“The Demon-Haunted World: Science as a Candle in the Dark”*, 1995

ACKNOWLEDGEMENTS

Eu gostaria de agradecer principalmente aos meus orientadores; professor Odylio Aguiar, professor Siong Heng e professora Iara Tosta por terem aceitado me orientar, por toda assistência e paciência no desenvolvimento da dissertação. Sem eles, esse trabalho não seria possível.

Aos pesquisadores da Colaboração Científica LIGO-Virgo-Kagra; Marco Drago, Dixeena Lopez, Gabriele Vedovato, Shubhanshu Tiwari e Andrea Virtuoso, pelo suporte técnico com o pipeline coerent WaveBurst e pelas dicas a respeito do trabalho.

Aos professores do INPE; José Carlos, Claudia Vilega, Rafael Nunes, Francisco Jablonski, Alexandre Wuensche, André Milone e João Braga, pelos valiosos ensinamentos transmitidos durante esses últimos dois anos e por me introduzirem a essa área científica fascinante.

À minha mãe Wanderléa e meus irmãos João, Antônio (Toh) e Tathiane, que são minha base e meu porto seguro. Ao meu pai Antônio e minha avó Teresa, por sempre me apoiarem na empreitada acadêmica. Aos amigos, pelos momentos de descontração, apoio, motivação e pelas boas histórias, mesmo em tempos difíceis.

Aos meus colegas de pós-graduação, Camilla, Juliédson e Ana Luiza, pelos momentos compartilhados, pelo suporte e boas risadas.

À CAPES, pelo apoio financeiro.

ABSTRACT

The Brazilian Gravitational Wave (GW) detector Mario Schenberg was conceived in the early 2000s and operated until 2016, when it was dismantled. It consists of a spherical resonant mass antenna sensitive to GW signals from 3150 Hz to 3260 Hz, and for this frequency range it has an "ultimate" sensitivity comparable to that achieved by Advanced LIGO detectors during the third observational run (O3). It is in the interest of part of the Brazilian scientific community that this project does not come to an end. The Schenberg project can contribute to the international gravitational wave research. Assuming the similar sensitivities between those detectors, this dissertation aims to search for short GW burst signals in the O3 data of Advanced LIGO in which its results help to characterize the advantage of reassembly of the Schenberg antenna. Here I perform a search for signals with milliseconds to a few seconds without making assumptions about their morphology, polarization, and arrival sky direction. The data were analyzed with the coherent WaveBurst pipeline (cWB) with frequencies from 512 Hz to 4096 Hz and the search targets only signal that have bandwidth overlapping the Schenberg frequency band. No statistically significant evidence of GW bursts during O3 was found. This result was used to feature the search efficiency in identifying different signal morphologies and establish upper limits on the GW burst event rate as a function of its strain amplitude. It was also possible to estimate a distance to detect a set of waveforms from potential astrophysical sources. This search, and consequently Schenberg, is sensitive to sources emitting isotropically $5 \times 10^{-6} M_{\odot} c^2$ in GWs from a distance of 10 kpc with 50% detection efficiency and with a false alarm rate of 1/100 years. The feasibility of detecting f-modes of neutron stars excited by glitches was also investigated. Based on rough estimates, Schenberg would need at least 5.3 years of observation run to get a single detection of this type of signal, given $E_{glitch} \approx 10^{-10} M_{\odot} c^2$.

Keywords: Gravitational Wave. Data Analysis. LIGO. coherent WaveBurst. Schenberg. Bursts.

BUSCA POR RAJADAS DE ONDA GRAVITACIONAL NOS DADOS DO LIGO NA FAIXA DE SENSIBILIDADE DO SCHENBERG

RESUMO

O detector brasileiro de Ondas Gravitacionais (OGs) Mario Schenberg foi concebido no início dos anos 2000 e operou até o ano de 2016, quando foi desmontado. Ele é composto por uma antena de massa ressonante esférica sensível a sinais de OGs de 3150 Hz a 3260 Hz, e para essa faixa de frequência possui uma máxima sensibilidade de projeto comparável a atingida pelos detectores Avançados LIGO durante a terceira corrida observacional (O3). É de interesse de parte da comunidade científica brasileira que seu projeto não se encerre. A eventual remontagem do detector brasileiro se encaixa em um contexto frutífero de expansão da pesquisa internacional em OGs devido ao recente e progressivo número de detecções pelos interferômetros LIGO. Partindo do pressuposto da equivalência da sensibilidade entre esses detectores, essa dissertação se objetiva em buscar sinais de rajadas curtas de OGs nos dados de O3 do LIGO Avançado em que seus resultados ajudam a caracterizar a vantagem da remontagem da antena Schenberg. É uma busca por sinais com duração de milissegundos até alguns segundos sem fazer suposições sobre sua morfologia, polarização e direção de chegada do céu. Os dados foram analisados com o coerent WaveBurst pipeline (cWB) com frequências de 512 Hz a 4096 Hz e foram alvos da busca apenas sinais que possuem largura de banda sobreposta a banda de frequência do Schenberg. Não foram encontradas evidências estatisticamente significativas de rajadas de OGs durante O3. Esse resultado foi usado para caracterizar a eficiência da busca em identificar diferentes morfologias de sinais e também para estabelecer limites superiores na taxa de eventos de rajadas de OG em função da sua amplitude de deformação. Também foi possível estimar uma distância com a qual é possível detectar um conjunto de formas de onda de potenciais fontes astrofísicas. Essa busca e consequentemente o Schenberg, são sensíveis a fontes emitindo isotropicamente $5 \times 10^{-6} M_{\odot} c^2$ em OGs de uma distância de 10 kpc com 50% de eficiência de detecção e com uma taxa de falso alarme de 1/100 anos. Também foi investigada a viabilidade de detecção de modos fundamentais de oscilações em estrelas de nêutrons excitadas por glitches. Baseado em estimativas aproximadas, o Schenberg precisaria de pelo menos 5,3 anos de observação para obter uma única detecção desse tipo de sinal, considerando $E_{glitch} \approx 10^{-10} M_{\odot} c^2$.

Palavras-chave: Ondas Gravitacionais. Análise de dados. LIGO. coherent WaveBurst. Schenberg. Rajadas.

LIST OF FIGURES

	<u>Page</u>
2.1 This figure shows the effect of the + and × polarizations in the ring of free-falling test masses located in the (x, y) plane of a local inertial system by a monochromatic gravitational wave that travels along the z direction with $w = 2\pi/T$	11
2.2 On the top, the figure shows the gravitational wave strain amplitude estimated for the GW150914 event in one of the LIGO detectors. The waveform is followed by a visual representation of the system dynamics. On the bottom, the evolution in time for BBH separation (in R_s units) and the effective relative velocity are displayed, given by the post-Newtonian parameter $v/c = (GM\pi f_{GW}/c^3)^{(1/3)}$	15
3.1 Instrumental schematic of the Mario Schemberg Spherical Antenna.	20
3.2 The pink line represents the Schenberg strain noise spectral density.	21
3.3 The left part shows the layout of an Advanced LIGO detector. The Michelson interferometer arms are enhanced by resonant cavities, which increase the optical power in the arms and improve sensitivity. The dynamic of optical power in different interferometer elements are represented by the red light’s opacity level on the figure. On the right is a schematic of the different stages of the test masses suspension system to minimize mechanical noises.	22
3.4 Representative amplitude spectral density of the three interferometric detectors’ strain sensitivity during different times of the third observational run first part (O3a). It is possible to see the detectors’ most sensitive frequency band is between 100 Hz and 300 Hz.	23
3.5 Representation of the steps to visualize the GW150914 event from the raw LIGO-Hanford data. Applying a Tukey window function, followed by whitening from an estimate of noise spectral amplitude and applying a bandpass filter of [35 - 350] Hz in this case.	26
3.6 The main steps of LIGO–Virgo data processing. The stages of GW searches are represented in the blue box and are usually covered by search pipelines.	27
3.7 The selection of pixels that have excess power from the LIGO-Hanford data of GW150914. Each column is in a different resolution in the time-frequency representation.	33

3.8	On the left is the waveform reconstruction in the time-frequency plane of the GW150914 event after maximizing the likelihood. The cWB reconstruction of GW150914 in the frequency domain (red line) from a posterior signal sample (black line) is on the right.	33
4.1	The Schenberg design strain sensitivity for the overall system (not only a single mode channel), with a non-degenerate sphere, in a cryogenic system at 0.1 K compared to the representative spectral strain sensitivity of the LIGO Hanford (29 April 2019 11:47 UTC), LIGO Livingston (5 September 2019 20:53 UTC) and Virgo (10 April 2019 00:34 UTC) during O3. The Schenberg sensitivity curve for the initial version of Schenberg (with the present electronics available in the project) is not as good as the O3 aLIGOs sensitivity curves, however supposing an advanced version of Schenberg (aSchenberg) with state of art electronics and outstanding mechanical and electric Qs, in such a way that the series (electronic) and thermal noises would be substantially decreased, the Schenberg sensitivity would approach the standard quantum limit (flat spectrum, represented by the dashed black line). However, this "ultimate" Schenberg sensitivity is already achieved in O3 by the two LIGO interferometers, so analyzing the LIGO O3 data in the Schenberg bandwidth of sensitivity is an excellent measure to evaluate what are the chances of gravitational wave detection by an aSchenberg with "ultimate" sensitivity. The detector model used to construct the Schenberg sensitivity curve is not yet published.	37
4.2	Functional diagram showing the main stages of the cWB pipeline.	39
4.3	Schematic representation of the time shift procedure for background estimation. The zero-lag (not shifted stream) coincidence situation between the LIGO Livingston (LLO) and Hanford (LHO) detector data is illustrated at the top. In this case, a GW signal, represented by the symbol X, can be found within the time coincidence window, i. e., a few ms. At the bottom, the LHO data stream temporally shifted when compared to the LLO data. In this time-lag configuration, the signal due to excess power of the noise (represented here by circles) and within the coincidence time window is described as a background trigger.	43

4.4	The magnitude distribution of coherent background triggers, characterized by the coherent network SNR plotted versus the central frequency values. It is possible to see more significant triggers about the other data chunks from the beginning of the first half of O3 until May 16, 2019 (chunk 1). The loudest ones grows as the frequency increases and justify the cut produced at $f_0 > 3400$ in order to obtain a cleaner distribution.	45
4.5	The magnitude distribution of all coherent background triggers in O3.	46
4.6	The distribution of zero-lag triggers burst detection statistic, characterized by the coherent network SNR, as a function of the reconstruct central frequency values. Most of the population of identified events has a central frequency outside the Schenberg band.	47
4.7	The time distribution of candidate events over the entire O3 livetime with the respective values of η_c	47
4.8	The FAR versus ranking statistic η_c for all observation periods of O3: chunk 1 (top), chunk 2 (middle), and chunk 3 (bottom).	50
4.9	The cumulative number of background triggers versus IFAR for O3b. Since we are looking at the background triggers represented by the blue triangles, they should fall precisely on the expected line of the background. The green area shows the one, two, and three-standard deviation errors on the expected value of the background estimate, assuming a Poisson distribution.	51
4.10	The cumulative number of events above a threshold IFAR, for zero-lag coincident events, shown as red triangles. The expected background (given the analysis time by definition) is shown as a solid black line.	53
4.11	The cumulative number of zero-lag triggers versus IFAR for all O3. The vertical blue lines represent the minimum IFAR values for each chunk and the positions of the kinks.	54
4.12	The cumulative number of zero-lag triggers versus the combined IFAR for all O3 after normalization.	55
4.13	Representative plot of the efficiency curve for two Ring-Down injections in O3a epoch.	61
4.14	The GW-burst emitted energy expressed in units of solar masses which correspond to 50% detection efficiency at an $\text{IFAR} \geq 100$ years, for standard-candle sources emitting at 10 kpc for the waveforms listed in Table 4.5 into the Schenberg band. It is expected that the behavior of the RDC τ 050 and RDC τ 005 waveforms will follow the same frequency dependence as RDC τ 100.	63

4.15	The minimum distance, in kiloparsecs (kpc), for the waveforms listed in Table 4.5, for detection efficiencies of 10%, 50% and 90% at an IFAR ≥ 100 years and $E_{GW}^{iso} = 1 \times 10^{-6} M_{\odot} c^2$	64
4.16	Upper limits of gravitational-wave burst event rate at 90% confidence as a function of the strain amplitude h_{rss} for Ring-Down waveforms with central frequency in the Schenberg band [3150-3260] Hz. The results include both O3a and O3b epochs.	66
4.17	Upper limits of gravitational-wave burst event rate at 90% confidence as a function of the strain amplitude h_{rss} for Sine-Gaussian waveforms with central frequency in the Schenberg band [3150-3260] Hz.	67
4.18	Normalized probability density distribution of Galactic neutron stars at 30kpc.	69
4.19	The normalized cumulative distribution function of Galactic neutron stars at 30kpc.	70
4.20	The number of f-mode events per year, as a function of glitch energy for the estimated population of Galactic neutrons stars and pulsars. The y-axis goes up to the upper limit value for burst rate at 50% detection efficiency (which is ~ 8.6 <i>events/year</i> according Figure 4.16), and it can be interpreted roughly here as an upper limit in the energy value of f-modes generated by NS glitches.	72

LIST OF TABLES

	<u>Page</u>
4.1 O3 calibration epochs, the maximum 1σ , median excursions of response from unity magnitude and zero phases in the frequency band 512–4096 Hz.	41
4.2 Background livetime for the different epochs of O3.	44
4.3 Set of Sine-Gaussian waveforms injections.	59
4.4 Set of Ring-Down waveforms injections.	59
4.5 Values of h_{rss} in units of $10^{-22} \text{ Hz}^{-1/2}$ for 10%, 50% and 90% detection efficiency in O3a and O3b at the chosen FAR threshold of 1/100 years. .	61
A.1 Significance parameters of zero-lag triggers of chunk 1.	85
A.2 Significance parameters of zero-lag triggers of chunk 2.	85
A.3 Significance parameters of zero-lag triggers of chunk 3.	86

CONTENTS

	<u>Page</u>
1 INTRODUCTION	1
2 GRAVITATIONAL WAVES	5
2.1 Brief concepts of general relativity	5
2.2 Linearized field equations	7
2.3 Plane gravitational waves	9
2.4 Sources of gravitational waves	11
2.4.1 Gravitational waves from Compact Binary Coalescence (CBC)	13
2.4.2 Continuous gravitational waves	15
2.4.3 Gravitational-wave bursts	16
2.4.4 Stochastic gravitational waves	17
3 EXPERIMENTAL FEATURES AND DATA ANALYSIS	19
3.1 Detectors	19
3.1.1 Mario Schenberg spherical antenna	20
3.1.2 LIGO/Virgo interferometers	21
3.2 Analysis of LIGO-Virgo data	24
3.3 Coherent analysis	28
3.3.1 The coherent WaveBurst pipeline	30
4 ALL-SKY SEARCH FOR GRAVITATIONAL-WAVE BURSTS AT THE SCHENBERG BAND	35
4.1 Motivation	35
4.2 The search configuration	38
4.3 Data set	39
4.4 Analysis procedure	41
4.4.1 Background analysis	42
4.4.2 Zero-lag analysis	46
4.4.3 Detection statistics	48
4.4.3.1 Significance of candidate events	48
4.4.3.2 Expected and observed results	51
4.4.3.3 False alarm probability analysis	56
4.5 Astrophysical interpretation of the results	56

4.5.1	Search sensitivity	56
4.5.1.1	<i>Ad hoc</i> waveforms set	58
4.5.1.2	Efficiency analysis	59
4.5.2	Detection range	62
4.5.3	Upper limits	64
4.5.4	Detectability of f-modes	67
5	CONCLUSIONS	73
	REFERENCES	77
	APÊNDICE A	85
A.1	Detection parameters of zero-lag triggers	85

1 INTRODUCTION

In all its vast configuration, light manifests itself as the most significant source of information to study the universe. Examining its singularities, we can discover fantastic things about the place we inhabit. Until recently, light, cosmic rays and neutrinos were the only sources of information to study the intangible universe. The deep understanding of the nature of electromagnetic radiation, the interaction with matter, the production mechanisms, and its spectrum allowed the expressive development of knowledge for different phenomena and nature events.

This context was disturbed on September 14, 2015, with the first detection of a Gravitational-Wave (GW) signal. This signal, named GW150914, was generated by the coalescence and merger of two stellar black holes (ABBOTT et al., 2016c). It was detected by the Laser Interferometer Gravitational-wave Observatory (LIGO), composed by two detectors in different regions of the United States of America, one in Hanford, in Washington state, and the other in Livingston, Louisiana. The knowledge of this astrophysical event was exclusively possible through information from Gravitational Waves. Therefore, the first detection established a new window to study the universe, generating significant consequences in astronomy and physics fields.

The GWs can provide detailed information on the coherent bulk motion of matter that induces ripples in space-time geometry. On the other hand, electromagnetic waves usually offers spectrum information about individual atoms, molecules, and charged particles; however, they cannot provide direct details from some astrophysical objects' dense core. Therefore, together they can provide a rich overview of astrophysical events.

On August 17, 2017, the GW170817 signal coming from the inspiral and merger of two neutron stars was identified in the LIGO detectors with the participation of Virgo detector, placed in Italy (ABBOTT et al., 2017b). This event generated electromagnetic counterparts in different spectrum bands identified by 70 observatories arranged on Earth and in space. The coincident detections from different information settled a GW-multimessenger study of the event, providing unique and valuable insights into the properties and processes of the physical universe (MÉSZÁROS et al., 2019). Currently, ninety GW events are cataloged and were identified over three LIGO and Virgo observational runs (ABBOTT et al., 2019b; ABBOTT et al., 2020b; ABBOTT et al., 2021c; ABBOTT et al., 2021d). The progressive increase in the number of detections indicates good prospects for the future of Gravitational Wave Astro-

physics.

The international scenario of experimental research in Gravitational Waves had the active participation of Brazil in recent years through the Mario Schenberg antenna. The Schenberg is a spherical resonant mass detector of Gravitational Waves that was dismantled at the Physics Institute of the University of São Paulo in 2016 after executing its last observational run in 2015 (OLIVEIRA; AGUIAR, 2016). However, there is a great interest by part of the Brazilian scientific community that this project does not end. The development of a national project like the Brazillian antenna creates a favorable environment for the maturing of the recent field of Gravitational Wave Astrophysics, the training of researchers in the experimental and data analysis areas, placing Brazil in a more active role of international cooperation for the advance of this study field.

Resonant mass detectors as Schenberg, typically cover a small frequency band and achieve lower sensitivities when compared to the current interferometric detectors such as LIGO and Virgo (MAGGIORE, 2007). It is one of the reasons why all detections of GW signals identified to date have been through interferometric detectors, despite efforts to detect gravitational waves beginning in the 1960s using resonant mass detectors. In this regard, the possibility of detecting Gravitational Waves by another physical principle, such as resonant masses, becomes a great scientific interest and starts to contribute for the inevitable expansion of this scientific field can be structured from increasingly consistent data.

Given the perspective briefly portrayed, the present work tries to produce arguments to answer (although partially) the following question: From a scientific point of view, is the reconstruction of the Schenberg antenna at INPE advantageous? A direct way of approaching this problem is to verify the possibility of detecting GW signals by the Schenberg antenna within the features of its "ultimate" sensitivity. The identification of significant signals would be used as motivation (including financial support) for the Schenberg detector's reassembly and the possibility of detection of GW by another physical detection principle. As the detector is dismantled, we can get some indication using the data from the last experimental run (O3) of the LIGO detectors. It can be done since the Schenberg ultimate sensitivity is comparable to the interferometer sensitivities in the [3150-3260] Hz band in this experimental run.

This work aims to look for short-duration gravitational transients (up to a few seconds of duration), arriving from all-sky with some measurable energy within the Schenberg band. The search uses the coherent WaveBurst pipeline that explores

GW signatures without prior knowledge of signal morphology covering many waveform possibilities. Finally, it is possible to obtain astrophysical interpretations of the results, even the null detection case, by characterizing the search sensitivity from a detection efficiency study. Therefore, the present dissertation goes through the methodological data analysis challenges of interferometric detectors and places it in consonance with a national project with great research potential, the Schenberg antenna.

2 GRAVITATIONAL WAVES

2.1 Brief concepts of general relativity

General Relativity was developed at the beginning of the 20th century and published by Einstein in a couple of articles in 1915. It brings a new understanding of gravitational interaction, which was previously dictated by classical mechanics formalism and interpreted as a Newtonian force. Despite describing the solar system and astronomical phenomena successfully in general, Newtonian gravitation fails under extreme conditions. Also, it is not concerned with describing more specific features of gravitation, such as the speed in which the gravitational force propagates, for example.

Based on those aspects, the General Relativity theory was built from the incorporation of five physical principles that underpinned all its development (D'INVERNO, 1992), they are:

- Mach's Principle;
- principle of equivalence;
- principle of covariance;
- principle of minimal gravitation coupling;
- correspondence principle.

The resulting theory of these concepts is filled with new interpretations of the natural phenomena, mainly of the gravitational ones, which are no longer explained as a Newtonian force consequence. Instead, it is a result of the spacetime geometry and how its curvature causes a relative acceleration between bodies. Einstein synthesized his theory in the so-called equation of General Relativity for Gravitation or Einstein's Field Equations, written in a tensorial form as requires of covariance principle:

$$G_{\mu\nu} = \kappa T_{\mu\nu}, \tag{2.1}$$

where the indexes μ and ν run over the four coordinates of space and time. If we have repeated indexes they will follow the Einstein convention of implicit summation.

The left part of the Equation 2.1 is called the Einstein Tensor ($G_{\mu\nu}$) and carries the spacetime geometry features. The right part comprises the energy-momentum tensor ($T_{\mu\nu}$) that carries matter (energy) information and, therefore, is the source term in the field equations. The proportionality constant κ , also called the coupling constant, is determined by the principle of correspondence with Newtonian theory in the appropriate limits. This equation shows how matter generates spacetime curvature since spacetime's curvature is connected to matter distribution. A more explicit form of Equation 2.1 is:

$$R_{\mu\nu} - \frac{1}{2}g_{\mu\nu}R = \frac{8\pi G}{c^4}T_{\mu\nu}, \quad (2.2)$$

where $R_{\mu\nu}$ is the Ricci curvature tensor, $g_{\mu\nu}$ is the spacetime metric, G is the gravitational constant, and c is the speed of light in vacuum.

In other words, the local distribution of matter always generate $G_{\mu\nu}$, a geometric object composed by $R_{\mu\nu}$ (a Riemann tensor contraction) and $g_{\mu\nu}$ (a tool that allows one to compute vector products, distances, times, and allows the change of index positions) that comprises the spacetime curvature aspect, and this curvature information produces the relative acceleration of geodesics. J. A. Wheeler (1998) explains the connection of these terms in a simple form: "Matter tells space how to curve, and space tells matter how to move."

The gravitational phenomena described in an elegant form with this rich mathematical formalism provides a powerful tool to explain and predict extreme physical situations in the universe: it rules the movement of planets in the solar system, including the precession of Mercury; governs the deflection of light by stars and galaxies, and explains the gravitational lens effect; in stellar evolution, describes the collapse of a high mass star to form a black hole; establishes the structure of a compact object with symmetrical isotropic material (like a neutron star); in cosmology, governs the expansion and re-contraction of the universe; and many other events the universe contemplates (MISNER et al., 1973).

Our interest is to study one of the most intriguing (and hard to confirm) consequences of this theory. A hundred years ago, Einstein mathematically described that accelerated mass movement causes fluctuations in spacetime and it is propagated in the form of a wave at the speed of light; i.e., energy-momentum movement induces ripples in the curvature of spacetime, the definition of Gravitational Waves (GW).

2.2 Linearized field equations

The mathematical description of gravitational waves is a highly complex problem when examined with all General Relativity Theory perspectives. The Einstein's field equations are non-linear, therefore, they do not possess a principle of superposition (D'INVERNO, 1992). Also, with spacetime considerably curved, the Riemann tensor calculation involves second-order partial differentials with complicated solutions. An alternative to overcome this difficulty is to linearize the field equations. That will be possible in the condition of a weak field regime, namely the Minkowski flat spacetime with small disturbances, as follows:

$$g_{\mu\nu} = \eta_{\mu\nu} + h_{\mu\nu}, \quad (2.3)$$

which $\eta_{\mu\nu} = \text{diag}(-, +, +, +)$ is the Minkowski tensor and $h_{\mu\nu}$ represents a small perturbation of the spacetime metric, i. e., $|h_{\mu\nu}| \ll 1$.

From the Astrophysical outlook, this type of approach is consistent because an enormous amount of energy is required to produce a significant curvature of spacetime when analyzing the constants' magnitude of Equation (2.2). Besides, significant deformations of spacetime would be mitigated by the events' cosmological distances that can generate them.

When examining the outcomes of this metric choice it is possible to obtain linearized Einstein Equations by neglecting the second-order terms due to the slight perturbation of $h_{\mu\nu}$. The Christoffel symbols measure the extent to which coordinates deviate from (flat) straight lines along the spacetime grid and it is given by

$$\Gamma_{\mu\nu}^{\rho} = \frac{1}{2}g^{\rho\lambda} (\partial_{\mu}g_{\nu\lambda} + \partial_{\nu}g_{\lambda\mu} - \partial_{\lambda}g_{\mu\nu}) = \frac{1}{2}\eta^{\rho\lambda} (\partial_{\mu}h_{\nu\lambda} + \partial_{\nu}h_{\lambda\mu} - \partial_{\lambda}h_{\mu\nu}). \quad (2.4)$$

The partial derivative of components $\partial/\partial x^{\mu}$ is represented by the notation ∂_{μ} . In the weak-field limit, the linearized Riemann curvature tensor, written conveniently with the indexes lowered by the Minkowski metric, is written in the form (MAGGIORE, 2007):

$$R_{\mu\nu\rho\sigma} = \frac{1}{2} (\partial_{\nu}\partial_{\rho}h_{\mu\sigma} + \partial_{\mu}\partial_{\sigma}h_{\nu\rho} - \partial_{\mu}\partial_{\rho}h_{\nu\sigma} - \partial_{\nu}\partial_{\sigma}h_{\mu\rho}), \quad (2.5)$$

thus the Ricci tensor ($R_{\mu\nu}$) obtained by the contraction of the indexes μ and ρ in the Riemann tensor

$$R_{\mu\nu} = R^{\rho}{}_{\mu\rho\nu} = \frac{1}{2} (\partial_{\sigma}\partial_{\nu}h^{\sigma}{}_{\mu} + \partial_{\sigma}\partial_{\mu}h^{\sigma}{}_{\nu} - \partial_{\mu}\partial_{\nu}h - \square h_{\mu\nu}), \quad (2.6)$$

where it is possible to observe the symmetry of the indexes μ and ν . The trace of the perturbation tensor is defined in the equation above as $h = \eta^{\mu\nu}h_{\mu\nu} = h^{\mu}{}_{\mu}$ and the D'Alembertian operator $\square = \eta^{\mu\nu}\partial_{\mu}\partial_{\nu} = \partial^{\mu}\partial_{\mu} = -\partial_t^2/c^2 + \partial_x^2 + \partial_y^2 + \partial_z^2$ in the flat spacetime.

The Field equations are simplified when expressed using the so-called *trace reversed* tensor, defined as

$$\bar{h}_{\mu\nu} = h_{\mu\nu} - \frac{1}{2}\eta_{\mu\nu}h. \quad (2.7)$$

The tensor is called *trace reversed*, since its trace is written $\bar{h} = \bar{h}^{\nu}{}_{\nu} = \eta^{\mu\nu}\bar{h}_{\mu\nu} = -h$. After these considerations and writing the Einstein's tensor components with a *trace reversed* perturbation, we have finally a linearized version of Equation (2.2), explicitly as:

$$\square\bar{h}_{\mu\nu} + \eta_{\mu\nu}\partial^{\rho}\partial^{\sigma}\bar{h}_{\rho\sigma} - \partial^{\rho}\partial_{\nu}\bar{h}_{\mu\rho} - \partial^{\rho}\partial_{\mu}\bar{h}_{\nu\rho} = -\frac{16\pi G}{c^4}T_{\mu\nu}. \quad (2.8)$$

Considering the gauge freedom it is possible to impose additional restrictions on the metric perturbation without changing its physical nature (CARROLL, 1997). A convenient choice, in this case, is the harmonic gauge that maintains the geometry features under mathematical transformations for any $\bar{h}_{\mu\nu}$ described in a coordinate system, when the following condition is imposed

$$\partial^{\nu}\bar{h}_{\mu\nu} = 0. \quad (2.9)$$

In the harmonic gauge, some terms of Equation (2.8) vanishes, and it is reduced to

$$\square\bar{h}_{\mu\nu} = -\frac{16\pi G}{c^4}T_{\mu\nu}, \quad (2.10)$$

where each component of $\bar{h}_{\mu\nu}$ satisfies a flat spacetime equation.

2.3 Plane gravitational waves

From the perspective of gravitational waves detection, there is an astrophysics interest for radiative solutions of Equation (2.10), i. e., in the vacuum ($T_{\mu\nu} = 0$), thus

$$\square \bar{h}_{\mu\nu} = 0, \quad (2.11)$$

where the D'Alembertian implies that wave-type solutions are propagated by space-time itself at the speed of light. The linearized field equations recover the superposition principle and a general solution can be written as the linear superposition of monochromatic plane waves that is defined as

$$\bar{h}_{\mu\nu} = \Re \left(A_{\mu\nu} e^{ik_\alpha x^\alpha} \right), \quad (2.12)$$

where $A_{\mu\nu}$ is complex amplitude and k^α is the wave vector composed by the gravitational wave angular frequency w in timelike component; $k^\alpha = (w/c, \vec{k})$. Placing the solution (2.12) into Equation (2.11), implies in

$$k_\alpha k^\alpha = \eta_{\alpha\beta} k^\alpha k^\beta = 0, \quad (2.13)$$

so the wave vector is null or lightlike, since the norm of the vector is zero and timelike component is $w/c = |\vec{k}|$. Further implications succeed from the harmonic gauge condition (2.9) in the solutions (2.12), resulting

$$k^\mu A_{\mu\nu} = 0, \quad (2.14)$$

that implies the amplitude of the plane gravitational wave is orthogonal to the direction of propagation. It is possible to insert additional conditions beyond the harmonic gauge for $\bar{h}_{\mu\nu}$, considering the numbers of independent components (MAGGIORE, 2007):

$$\bar{h}_{00} = 0, \quad \bar{h}_{\mu 0} = 0, \quad \bar{h}^i{}_i = 0, \quad \partial^j \bar{h}_{ij} = 0, \quad (2.15)$$

where the indexes i and j indicates the spatial coordinates. It is possible to see from the restrictions (2.15) that only spatial components do not vanish.

Once using these conditions, the trace $\bar{h} = 0$, so $\bar{h}_{\mu\nu} = h_{\mu\nu}$ according to Equation (2.7). The traceless requirement and the transverse solutions as demanded by the harmonic gauge define the so-called *transverse-traceless* gauge or TT gauge. The perturbation metric on this specific gauge is denoted by $h_{\mu\nu}^{TT}$.

Considering the symmetries and restrictions imposed by TT gauge, left two independent components representing the physical information of the plane wave (CARROLL, 1997). Assuming a plane monochromatic gravitational wave propagating in the z direction, that is, $k^\mu = (w/c, 0, 0, w/c)$ the nonvanishing components of $h_{\mu\nu}^{TT}$ are:

$$h_{xx}^{TT} = -h_{yy}^{TT} = \Re\left(A_+ e^{-iw(t-z)}\right); \quad (2.16)$$

$$h_{xy}^{TT} = h_{yx}^{TT} = \Re\left(A_\times e^{-iw(t-z)}\right), \quad (2.17)$$

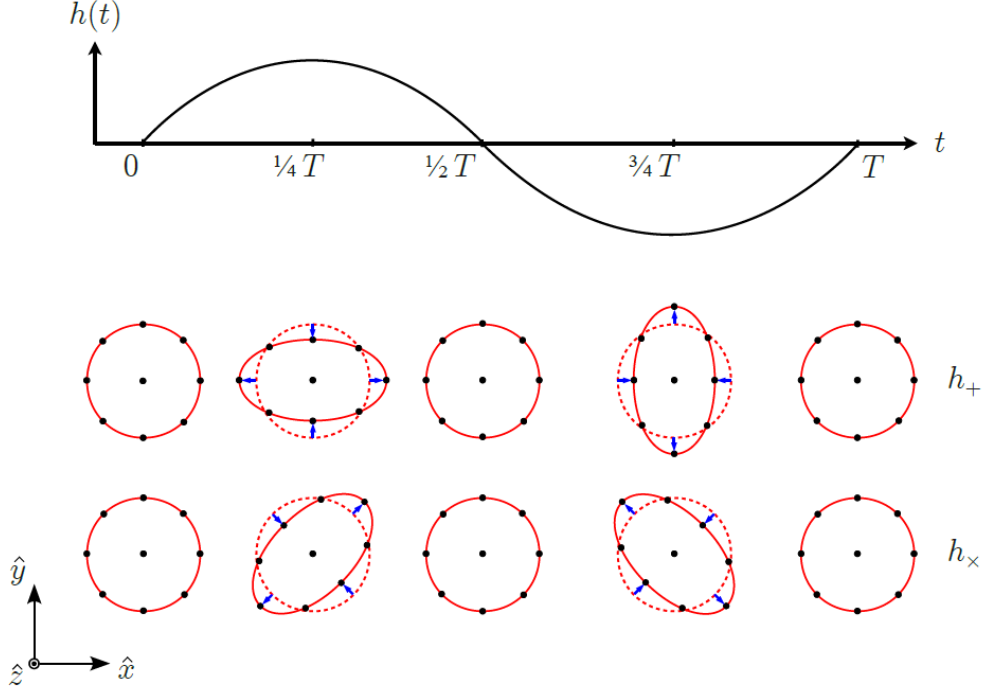
where amplitudes A_+ and A_\times represent the two independent polarization modes and are called *cross* and *plus* polarization amplitudes of gravitational-wave (MISNER et al., 1973). We can represent the perturbation tensor for this case, by the following matrix form:

$$\mathbf{h}_{\mu\nu}^{TT} = \begin{pmatrix} 0 & 0 & 0 & 0 \\ 0 & h_+ & h_\times & 0 \\ 0 & h_\times & -h_+ & 0 \\ 0 & 0 & 0 & 0 \end{pmatrix},$$

where the terms h_+ and h_\times represent the Equations (2.16) and (2.17) respectively.

The gravitational wave effect on the matter can be understood as the overlap of two oscillating tidal fields that propagate in vacuum at the speed of light. The separation direction of two test particles influences the altering impact of geodesic separation between them. Considering a ring of free-falling test masses located in the (x, y) plane of a local inertial system, a transverse passage of a gravitational wave induces the tidal effect in the direction of independent polarizations, as shown in Figure 2.1.

Figure 2.1 - This figure shows the effect of the $+$ and \times polarizations in the ring of free-falling test masses located in the (x, y) plane of a local inertial system by a monochromatic gravitational wave that travels along the z direction with $\omega = 2\pi/T$.



SOURCE: Tiec and Novak (2017).

2.4 Sources of gravitational waves

As mentioned in Section 2.2, regarding the constants of the Equation (2.10), the generation of gravitational waves must involve highly energetic events in the universe to imply a possibility of detection. Analytical solutions to Einstein's equations are also complicated to obtain for generic cases from astrophysical sources. It is possible to treat the radiative gravitational waves in the weak-field limit by studying the first order of emission mechanism of the source (CREIGHTON; ANDERSON, 2011) since many of them do not need to be fully investigated using relativity.

The structure of the perturbation tensor in the Einstein equations was described previously only evaluating the solution in a vacuum, without making assumptions about the source of this perturbation. General solutions of the linear Equation 2.10 can be obtained by a retarded time Green's function, like in the electromagnetism:

$$\bar{h}_{\mu\nu}(t, \vec{x}) = \frac{4G}{c^4} \int d^3x' \frac{1}{|\vec{x} - \vec{x}'|} T_{\mu\nu} \left(t - \frac{|\vec{x} - \vec{x}'|}{c}, \vec{x}' \right). \quad (2.18)$$

It is possible to reveal physical quantities, such as matter density, after expanding the energy-momentum tensor and redefinition of variables. Those mathematical steps can be seen in detail at [Maggiore \(2007\)](#).

Gravitational waves are produced by moving forms of mass-energy, just like electromagnetic waves are produced by moving electric charges. However, the lowest-order post-Newtonian approximation and the conservation laws of nature indicate that the emitted gravitational radiation follows the quadrupole formula ([SATHYAPRAKASH; SCHUTZ, 2009](#)). In particular, it is produced whenever the quadrupole moment of an energy distribution evolves non-linearly with time, that is:

$$\bar{h}_{ij}(t, \vec{x}) \simeq \frac{2G}{rc^4} \ddot{Q}_{ij}(t - r/c), \quad (2.19)$$

where r is the distance from the source (in the approximation to a far source $r \sim |\vec{x} - \vec{x}'|$), and the term $(t - r/c)$ indicates that expression is evaluated at a retarded time. Remark this definition is generalized to the *trace reversed* perturbation. An additional projection tensor can be used to represent this quantity in the TT gauge. The dots symbolize time derivatives, and the spatial tensor Q_{ij} is the quadrupole moment tensor defined by the equation:

$$Q_{ij} = \int x_i x_j \rho(t - r/c, \vec{x}) d^3x, \quad (2.20)$$

where ρ is the matter density. The Equation (2.19) is to be interpreted as a linearized gravitational wave in the distant almost-flat geometry far from the source, in the harmonic gauge ([SATHYAPRAKASH; SCHUTZ, 2009](#)).

In this context, the power radiated, or gravitational luminosity equation used for a wide variety of sources is given by

$$L_{GW} = \frac{G}{5c^5} \left\langle \ddot{Q}_{jk} \ddot{Q}_{jk} - \frac{1}{3} \ddot{Q}^2 \right\rangle, \quad (2.21)$$

where Q is the trace of the tensor Q_{jk} ([MISNER et al., 1973](#)) and the brackets indicate a

time average over several distinct periods of the gravitational waves. A more detailed description beyond the Newtonian limit includes posterior terms in post-Newtonian analysis (CREIGHTON; ANDERSON, 2011).

Many events can generate gravitational waves in the universe with amplitudes considerably capable to be detected. A gravitational wave signal eventually detected on Earth may come from a know or unknown source, and have a short, long, or continuous-time duration. Furthermore, the search for GW signals takes into consideration a modeled or unmodeled astrophysical phenomenon. These points are essential for searching signals, leading to the definition of four gravitational wave categories.

2.4.1 Gravitational waves from Compact Binary Coalescence (CBC)

A compact binary system is composed by two compact objects orbiting and getting closer to each other. It is typically constituted of neutron stars and black holes that may form: Binary Neutron Star (BNS), Binary Black Hole (BBH), or Neutron Star-Black Hole Binary (NSBH). Neutron Stars are remnants of a massive star's collapse and own the highest values of matter density in the observable universe. It comprises a typical mass of $1.4M_{\odot}$ in a sphere of 12 km radius, resulting in a gravitational acceleration on its surface 130 billion times greater than on the Earth's surface. In the stellar evolution theory, black holes are generated by the final collapse of even more massive stars. This cataclysmic event generates a spacetime configuration by an extremely compact mass where gravity is so intense it prevents anything, including light, from leaving. According to the mass, black holes are classified as stellar ($5 - 65M_{\odot}$) intermediate ($10^2 - 10^5M_{\odot}$) and supermassive ($10^5 - 10^9M_{\odot}$) which the mass-radius relation is given by the Schwarzschild radius ($R_s = 2GM/c^2$).

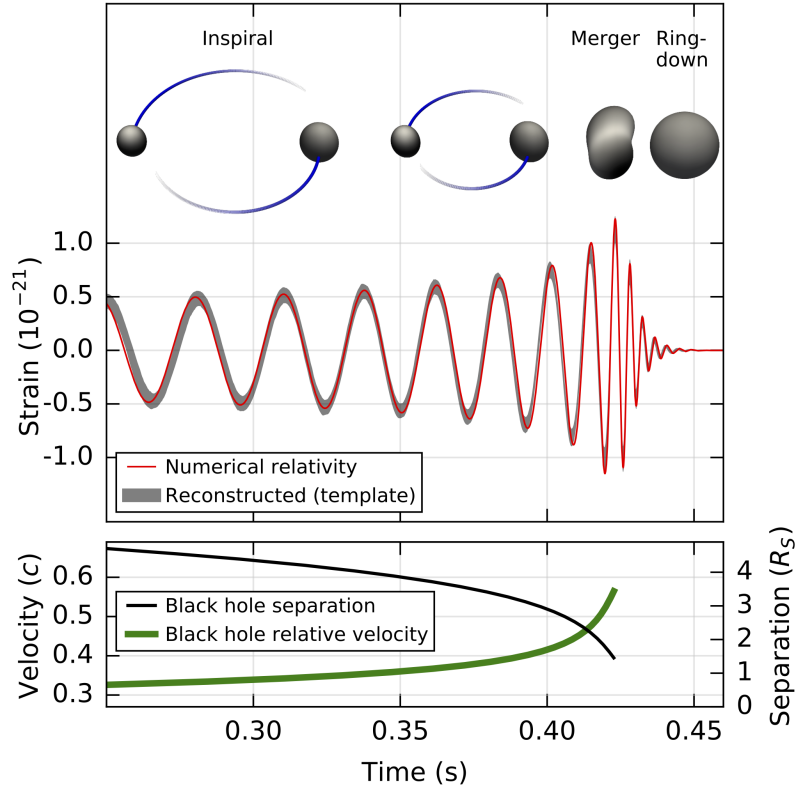
During the orbital movement of this system, there are gravitational wave emissions according to Equation (2.20). As the radiative gravitational waves dissipate the system's energy, the objects get closer, increasing the orbital frequency. The continuous decrease in the orbital period leads to more significant orbital energy losses due to gravitational waves and characterizes, over eons, the inspiral movement until the inevitable merger. This dynamic produces a signal of gravitational waves with a particular increase in amplitude and frequency ($f_{GW} = 2f_{orbital}$). For that reason, it is called a chirp signal.

As shown in Equation (2.20), a more massive system will have significant variations in the quadrupole moment. Therefore, it will generate more gravitational

waves resulting in a faster coalescence process. When evaluated at the same distance, Binary Black Hole systems emit gravitational waves with greater amplitude and less frequency, while Binary Neutron Star has lower amplitudes and higher frequencies. During the few peaks of the cycle that precedes the merger, the gravitational power radiated from BBH can compete with the steady luminosity of the entire universe (SATHYAPRAKASH; SCHUTZ, 2009). Usually, because of the enormous variations of the quadrupole moment and the source distance, only these few peaks have strain amplitude ($h(t)$ on Figure 2.1) enough to be detected, generating short-duration transient signals. Numerical simulations of BNS merger considering different equations of state (EoS), suggest that the frequency at peak emission may reach $f_{peak} > 3300$ Hz (ABBOTT et al., 2019c).

The compact coalescence processes are well understood and the resulting gravitational wave generation is currently modeled for different objects and orbital configurations. So far, all 90 detections of gravitational-wave signals have come from systems like these (ABBOTT et al., 2019b; ABBOTT et al., 2020b; ABBOTT et al., 2021c; ABBOTT et al., 2021d). The first gravitational wave event was defined as GW150914, a signal originated from the coalescence of a BBH system with $36M_{\odot}$ and $29M_{\odot}$ that merged and formed the final Black Hole with $62M_{\odot}$ mass. This event radiated $3M_{\odot}c^2$ in gravitational waves and was detected on September 14, 2015, at 09:50:45 UTC by two detectors of the Laser Interferometer Gravitational-Wave Observatory (LIGO) (ABBOTT et al., 2016c).

Figure 2.2 - On the top, the figure shows the gravitational wave strain amplitude estimated for the GW150914 event in one of the LIGO detectors. The waveform is followed by a visual representation of the system dynamics. On the bottom, the evolution in time for BBH separation (in R_s units) and the effective relative velocity are displayed, given by the post-Newtonian parameter $v/c = (GM\pi f_{GW}/c^3)^{1/3}$.



SOURCE: Abbott et al. (2016c).

2.4.2 Continuous gravitational waves

Continuous gravitational waves are characterized by monochrome signatures of constant amplitude from a compact object like a single fast-spinning neutron star (NS could spin over 700 Hz). According to the quadrupole moment, an ideal spherical mass distribution in rotation or whose radius oscillates uniformly, will not produce a gravitational wave. However, if the mass distribution has any kind of imperfection in its spherical shape (like "mountains") it will emit. Therefore, non-axisymmetric rotating neutron stars will generate gravitational waves. The time-stable asymmetry, together with the precise spin of a neutron star, is responsible for the signa-

ture of harmonic gravitational waves, with the same frequency and amplitude, since $f_{GW} = 2f_{spin}$. As a first approximation, the neutron star structure is composed of a superconductor fluid without viscosity. A more accurate description of the structure considers that fluid has oscillations, and gravitational waves can also be emitted due to the instability of different oscillation modes of these fluids (CREIGHTON; ANDERSON, 2011).

Another source of continuous gravitational waves is a compact binary system far away from the inspiral and consequent mergers situation. These systems have a constant orbital period considering the observational time scale. This leads to the generation of gravitational waves with very low frequency and amplitude.

These continuous sources can be modeled with high accuracy by a monochromatic sinusoid. Due to Earth's movement around the Sun along an observational time scale, it is essential to fix the frequency shift by the Doppler effect (RILES, 2017). Despite the easy modeling and searches involving known neutron stars, these signals have not been detected yet.

2.4.3 Gravitational-wave bursts

Bursts are unmodeled gravitational-wave signals which show excess power over a short duration, i.e., a fast and significant variation of a large quadrupole moment. This type of signal covers a wide variety of sources, making it difficult to establish its origin phenomenon.

Supernovae, usually caused by the final gravitational collapse of a massive star or the uncontrolled deflagration of a white dwarf by matter accretion, are among the most anticipated burst signals. Magnetars are neutron stars with a strong magnetic field that, when changes, induce unusual behaviors in their superficial structure, like short duration bursts. The production of short bursts of gamma rays and giant flares (rarely emitted) could associate with the generation of detectable gravitational waves (ABBOTT et al., 2019d). However, not enough is known about these phenomena and their gravitational details to anticipate a possible waveform.

In addition to these expected phenomena, the evidence of bursts signals might be related to events and sources of gravitational waves that have not yet been studied or perhaps not even imagined, covering a wide range of frequencies. The search for burst signals is indeed a search for unexpected information with the potential to alter our universe overview dramatically.

2.4.4 Stochastic gravitational waves

When a large enough number of gravitational wave emissions are superimposed in time and frequency, it may be impossible to distinguish the sources that compose it. In this case, the unresolved sources are interpreted as a single background. These gravitational waves arise from many combined random and independent events (such as continuous, bursts, compact binary coalescence...) from all over the universe, hence the name stochastic. By the central limit theorem, these random and independent events follow a Gaussian distribution in time and frequency (CREIGHTON; ANDERSON, 2011).

Stochastic gravitational waves can be remnants from the primordial universe. Between them, those produced by the Big Bang represent a gravitational analog of the cosmic microwave background (CMB) radiation. Studying the gravitational signatures of the Big Bang can provide valuable and unique information about the initial moments of an undiscovered universe. However, this type of signal has not yet been detected and will be the most difficult one, mainly due to the very low amplitude.

3 EXPERIMENTAL FEATURES AND DATA ANALYSIS

3.1 Detectors

As shown in the 2.3 Section, in the local inertial frame of free-falling masses, the passage of a gravitational wave through the masses generates relative accelerations between them. That induces strains in the particular directions of polarizations that can be evaluated over time as shown in Figure 2.1. Therefore, the passage of the gravitational wave deposits part of its energy when interacting with matter, allowing the possibility of detection. However, the weak interaction with matter and the typical very low amplitude also makes the GWs extremely hard to detect. The experimental challenge was the main reason so that the first detection of gravitational waves (the GW150914 event) took 100 years to become a reality after its theoretical prediction by Einstein.

Over the years, efforts have been made to detect gravitational waves by two different experimental principles: the resonant-mass and laser interferometry (MAGGIORE, 2007). The initial attempts at detecting gravitational waves were performed using a resonant bar antenna in the 1960s, the first type of resonant-mass detectors. In both types of detectors, the series noise components restrict the experimental sensitivity. A brief description of these physical detection principles are shown below.

Resonant-mass detectors: The tidal force caused by the passage of the gravitational wave induces movements in the resonant mass that depends on the frequency and amplitude. The resonant mass (antenna) will transform the energy weakly deposited by the passage of the gravitational wave into mechanical energy. Suppose the frequency of the deposited signal is close to the natural frequency of the antenna vibration. In that case, the mechanical system will resonate, increasing the amplitude of the oscillation movements. Secondary mechanical resonators assist in amplifying this effect. The mechanical vibration information is converted into electrical signals by transducers that generate the output information and then will be amplified analogically. The sensitivity range covers a short frequency band in these detectors ($\Delta f \sim 150$ Hz).

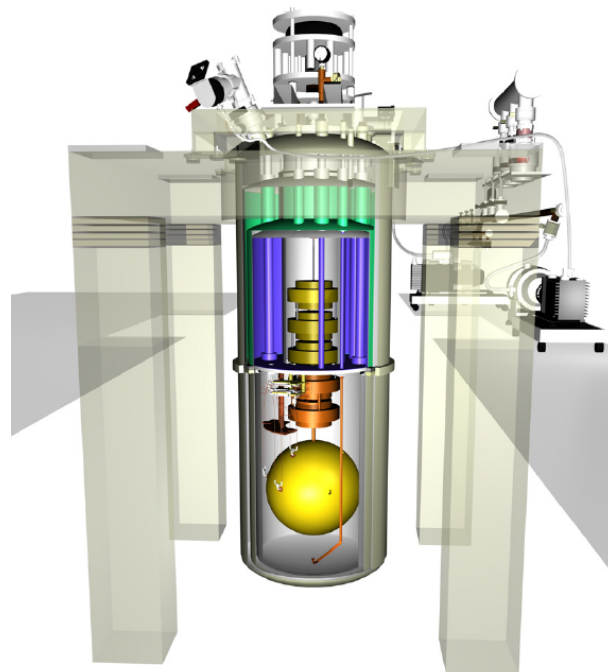
Interferometric detectors: Consists of a large-scale Michelson interferometer that is calibrated to cause destructive interference (dark fringe) of the laser light that is initially separated by a beamsplitter into the suspended mirrors (test masses) and is recombined on a photodetector. The gravitational wave passage changes the interference configuration after it interacts with the mirrors and produces differential

accelerations in the directions of the interferometer arms. Therefore, the measurement is based directly on monitoring the separation between the mirrors. Unlike resonant mass detectors, the sensitivity of laser interferometers covers a wide frequency range (few Hz to kHz).

3.1.1 Mario Schenberg spherical antenna

In more recent generations of resonant-mass detectors, instead of being composed of a bar resonant-mass, they were made as a spherical mass. One of these is the Brazilian Mario Schenberg antenna that remained in operation until 2015 at the Physics Institute of the University of São Paulo when it was dismantled. The spherical element has about 1150 kg of weight and 65 cm in diameter, made of copper-aluminum alloy with 94 % Cu and 6 % Al (AGUIAR et al., 2005). The sphere is held in a cryogenic chamber hung by a suspension mechanism as shown in Figure 3.1. Nine transducers are responsible for converting the mechanical vibration into an electrical signal that, later on, will be read for data analysis and searched for gravitational wave signal.

Figure 3.1 - Instrumental schematic of the Mario Schenberg Spherical Antenna.

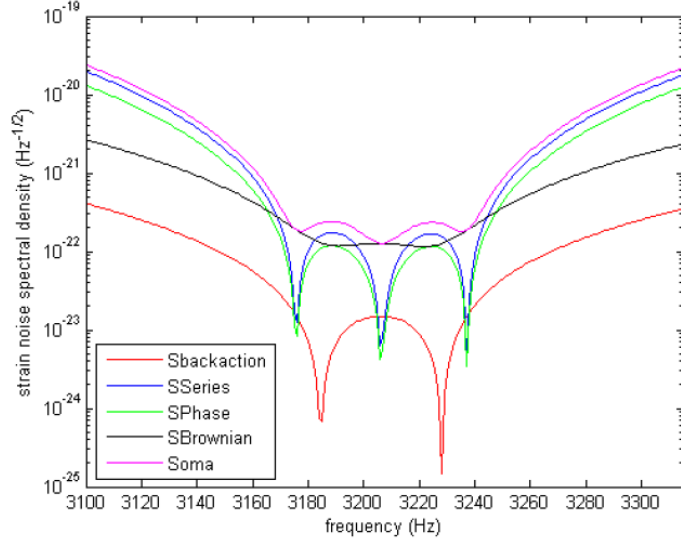


SOURCE: Costa et al. (2008).

With these instrumental features, experimental measurements combined with simu-

lations provide estimates of the design sensitivity of Schenberg Spherical Antenna as shown in Figure 3.2. Sensitivity is typically represented as strain noise spectral density (see Section 3.3). The Schenberg Antenna is expected to have the strain noise spectral density $\sim 10^{-22} \text{ Hz}^{1/2}$ (COSTA et al., 2008). However, the design sensitivity can be improved when considering a cryogenic system.

Figure 3.2 - The pink line represents the Schenberg strain noise spectral density.



SOURCE: Paula et al. (2014).

With this sensitivity it is possible to search for high-frequency GWs signals in the 3150 – 3260 Hz frequency bandwidth, such as burst signals from core-collapse in supernova events, magnetars flares, oscillations of neutron stars (f modes), and excitation of the first quadrupole normal mode of 4–9 M_{\odot} black holes. Also, gravitational-waves signals from the coalescence of neutron stars and/or black hole systems of 4–9 M_{\odot} . In addition to these sources, it is speculated the possibility of searching for exotic sources such as the rotation of strange matter stars and the inspiralling of mini-black hole binaries, if they exist (AGUIAR et al., 2012).

3.1.2 LIGO/Virgo interferometers

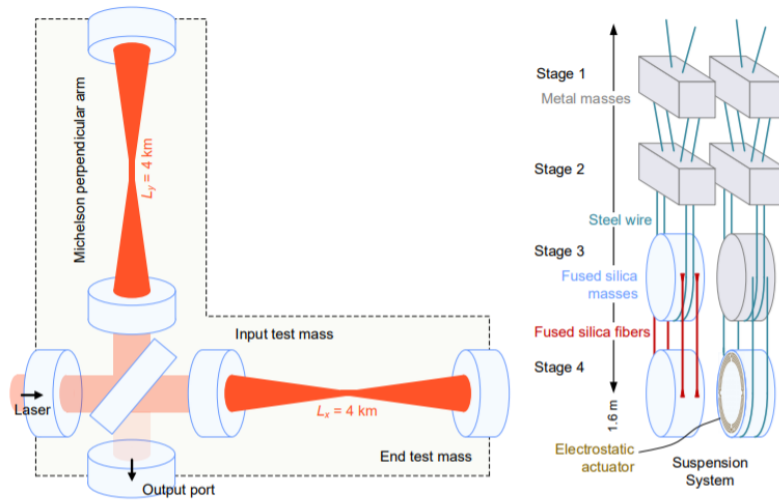
LIGO is a gravitational wave observatory composed by two laser interferometer detectors located in Hanford, in Washington state, and the other in Livingston, in Louisiana state in the United States of America. Each LIGO detector is a large Michelson interferometer with two equal arms perpendicular to each other in an

'L' shape with 4 km of extension, as shown the Figure 3.3. The interferometer mirrors functions as "free fall" test masses. Therefore, it is possible to measure the linear difference of these arms, which is proportional to the gravitational wave strain amplitude (ABBOTT et al., 2016b). This displacement caused can be expressed as a dimensionless quantity of the strain h (linear combination of h_+ and h_\times):

$$h = \frac{\Delta L}{L}, \quad (3.1)$$

where $\delta L_x - \delta L_y = \Delta L$ and $L = L_y = L_x = 4$ km in this case.

Figure 3.3 - The left part shows the layout of an Advanced LIGO detector. The Michelson interferometer arms are enhanced by resonant cavities, which increase the optical power in the arms and improve sensitivity. The dynamic of optical power in different interferometer elements are represented by the red light's opacity level on the figure. On the right is a schematic of the different stages of the test masses suspension system to minimize mechanical noises.

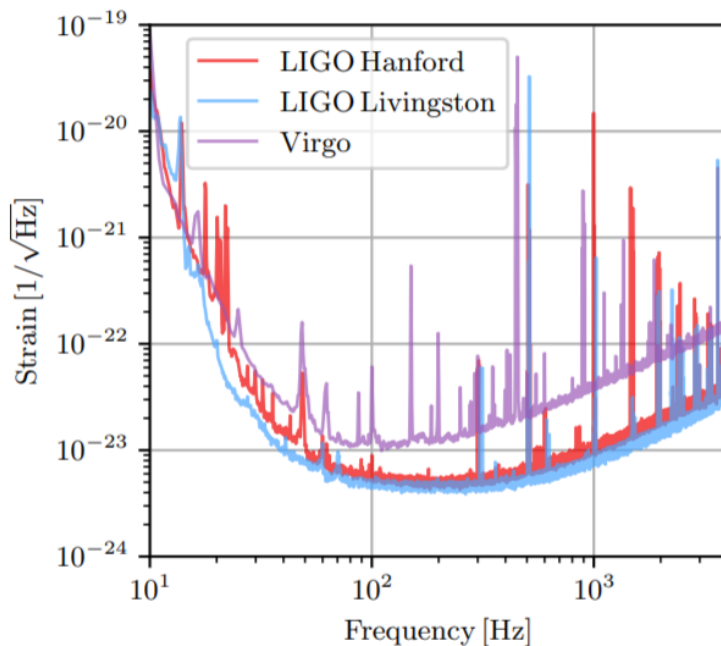


SOURCE: Abbott et al. (2016b).

There have been three observational runs with LIGO (O1, O2, and O3 runs) after an instrumental upgrade which caused a significant improvement in sensitivity and has come to be usually called Advanced LIGO. Virgo is also an interferometer based on the same principle of detection scheme. However, it has 3-kilometer-long arms and is located at the Cascina site near Pisa, Italy (ACERNESE et al., 2014). After a process of significant instrumental improvement, the Virgo detector (now Advanced Virgo or

aVirgo) joined with the two Advanced LIGO (aLIGO) interferometers at the end of O2 to form an international network of gravitational-wave interferometric detectors with great sensitivity. The last observational run, O3 (divided into O3a and O3b), carried from April 1st, 2019, to March 2020. All detected gravitational-wave events have had participation from at least one of these three detectors to date.

Figure 3.4 - Representative amplitude spectral density of the three interferometric detectors' strain sensitivity during different times of the third observational run first part (O3a). It is possible to see the detectors' most sensitive frequency band is between 100 Hz and 300 Hz.



SOURCE: Abbott et al. (2020b).

The interferometers network can identify several sources of gravitational waves since they cover an extensive frequency range with good sensitivity. The data generated by the observational runs are analyzed jointly by the LIGO and Virgo scientific collaborations, and after that, are available for open access at Gravitational Wave Open Science Center (LIGO SCIENTIFIC COLLABORATION AND VIRGO COLLABORATION, 2022).

The Advanced LIGO and Advanced Virgo are currently the highest sensitivity GW detectors as second-generation detectors. The third generation of ground-based interferometer detectors such as the Einstein Telescope (ET) and the Cosmic Explorer

(CE) will achieve a greatly improved sensitivity, expected to be more than ten times larger than the current ones (MAGGIORE et al., 2020; EVANS et al., 2021). It will increase the current detection rate and the potential for detecting events not yet observed. It is expected that in the 2030s, third generation GW detectors will be operational. In addition, there are projects in space, such as the Laser Interferometer Space Antenna (LISA) (BAKER et al., 2019). On the other hand, it will work at lower frequencies than ground-based interferometers, which will allow the investigation of different GW sources in the universe.

3.2 Analysis of LIGO-Virgo data

After going through a calibration process, the interferometer photodiodes output is expressed as a time series of the strain gravitational-wave amplitude data, with a sampling rate of 20000 Hz for Virgo and 16384 Hz for LIGO detectors data. In addition to strain data, hundreds of thousands of auxiliary channels record data from the experimental instruments as time series to monitor the detector and its environment. This process assists in identifying time periods with low data quality caused by different types of noise that can produce a long time of instability and also for recognizing short-duration transients (glitches) with an unknown origin that can mimic a GW signal (ABBOTT et al., 2020a). The generated time series $d(t)$ can be represented as the linear combination of the noise $n(t)$ and a GW signal $h(t)$:

$$d(t) = h(t) + n(t), \quad (3.2)$$

and the main problem of detection is distinguishing $h(t)$ from $n(t)$ since the signals are immersed in noise. This is a complex problem and requires a correct treatment of the statistical properties of $n(t)$. The noise in the LIGO-Virgo detectors is approximately stationary when treated in subsequent and finite segments of time, therefore a more useful approach is to work in the frequency domain, usually computed by Fast Fourier Transform (FFT) (BRACEWELL, 2000). The power spectral density (PSD) of the noise can be estimated by the ensemble average of the noise Fourier components (MAGGIORE, 2007):

$$\langle |\tilde{n}(f)|^2 \rangle = \frac{1}{2} S_n(f) T, \quad (3.3)$$

where $S_n(f)$ is defined as power spectral density of the noise, T is a chunk period

of the time series used to measure $\tilde{n}(f)$, which gives the resolution in frequency $\Delta f = 1/T$, and $\tilde{n}(f)$ is the Fourier transform of the time domain quantity $n(t)$ formally given by:

$$\tilde{n}(f) = \int_{-\infty}^{\infty} n(t)e^{-2\pi ift} dt. \quad (3.4)$$

The noise of a detector is usually expressed as $\sqrt{S_n(f)}$, which gives the amplitude of each frequency bin and is called spectral strain sensitivity, noise spectral amplitude or amplitude spectral density of noise, with dimensions $\text{Hz}^{-1/2}$ (y-axis on Figures 3.2 and 3.4). Representing the noise features with Equation 3.3 provides a helpful approach to deal with detection statistics related to signal-to-noise ratio (SNR) because the power spectral density of the noise is smoothed (reduces the variance) when calculated as the average of different realizations of $|\tilde{n}(f)|^2$, each properly normalized and equal duration T , separated by a sufficient time shift to break correlations of the subsequent data chunks. In return, this method of power spectrum compression degrades the frequency resolution (KLIS, 1989).

Eventual correlations between frequency bins and spectral leakage may occur due to the features of the Fourier transform in a finite time. To minimize that effect, the data chunks must pass through a window function with smooth extremes (such as the Tukey window function, for example) before being transformed from the time domain to the frequency domain. Another necessary procedure for the treatment of noise from the raw LIGO–Virgo data is the whitening. The Fourier coefficients $\tilde{d}(f)$ are divided by the spectral amplitude density of noise $S_n^{1/2}(f)$ to "normalize" the noise contribution in each frequency bin, ensuring that the data is not governed only by the region that holds the most noise amplitude. At the end of this step, the time series can be represented again in the time domain by the inverse Fourier transform:

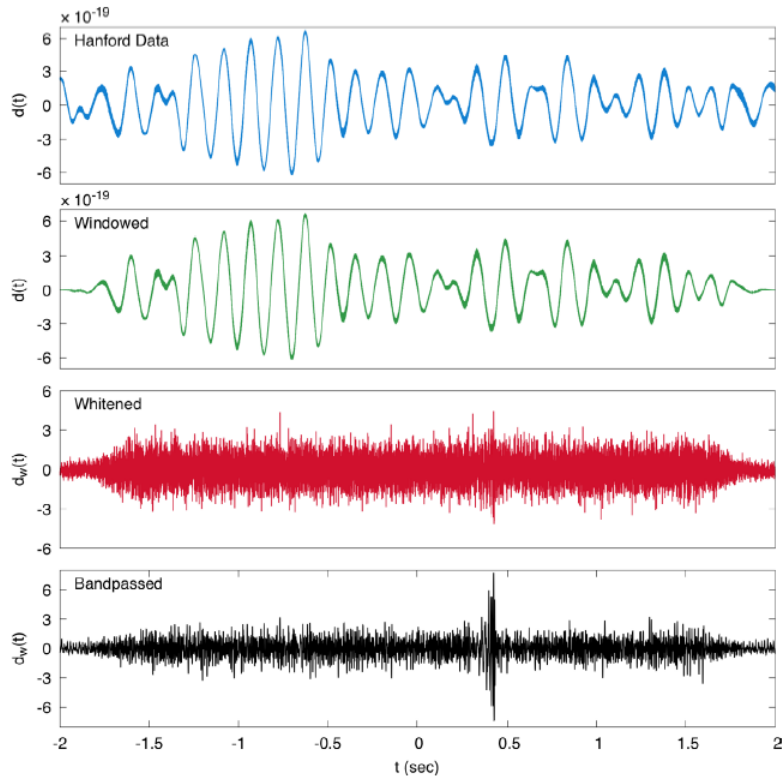
$$d(t) \xrightarrow{FFT} \tilde{d}(f) \xrightarrow{Whiten} \tilde{d}_W(f) = \frac{\tilde{d}(f)}{S_n(f)^{1/2}} \xrightarrow{iFFT} d_W(t) \quad (3.5)$$

This type of procedure is essential for LIGO/Virgo data that is highly dominated by low-frequency noise, as shown in Figure 3.4. To visualize the time series in a frequency of interest, the data goes through a bandpass filter that allows analyzing the data features only in the chosen frequency range, attenuating the noise contribution

outside the band.

The steps of initial data treatment that were briefly described can be seen in Figure 3.5. The raw data were collected from the LIGO-Hanford detector around 4 seconds of the GW150914 event, and after the application of the window function, whitening, and bandpass, it is already possible to note in the strain time series the chirp signal aspect from a compact binary coalescence, according to the waveform illustrated in Figure 2.2 for this event. The data processing steps do not need to be done in the described order. After transforming the data for the frequency domain, some gravitational wave search pipelines first apply the bandpass filter to minimize computational efforts, for example (ABBOTT et al., 2020a).

Figure 3.5 - Representation of the steps to visualize the GW150914 event from the raw LIGO-Hanford data. Applying a Tukey window function, followed by whitening from an estimate of noise spectral amplitude and applying a bandpass filter of [35 - 350] Hz in this case.

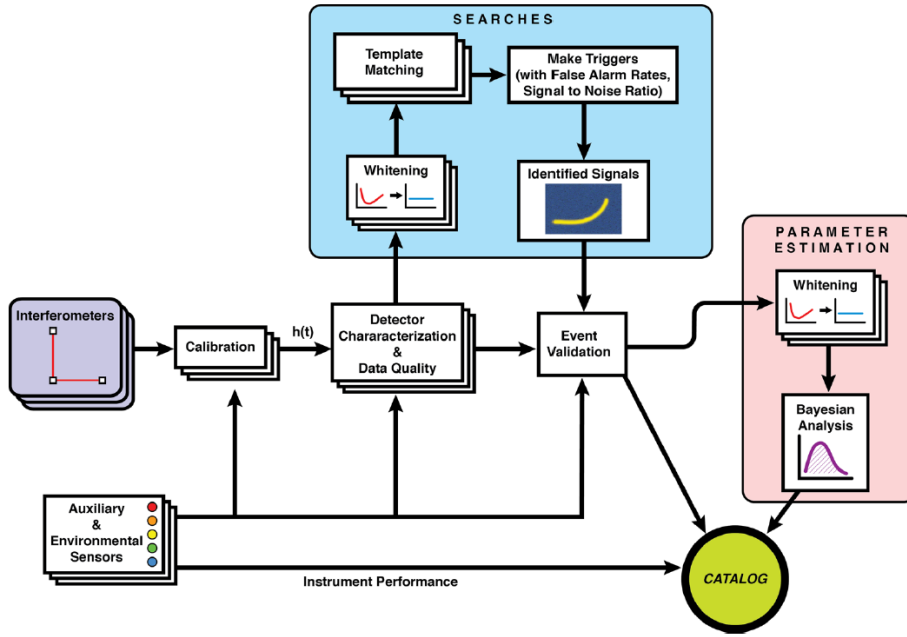


SOURCE: Abbott et al. (2020a).

After an initial treatment process of the data as shown here, searching for gravitational-wave signals can be approached by different forms and techniques. Fig-

Figure 3.6 schematically summarizes the main steps involved in the entire LIGO-Virgo detector data analysis process. The procedures highlighted in the blue box are those that involve the search and identification of gravitational wave signals exclusively. Each of the different search approaches has its statistical detection tests.

Figure 3.6 - The main steps of LIGO–Virgo data processing. The stages of GW searches are represented in the blue box and are usually covered by search pipelines.



SOURCE: Abbott et al. (2020a).

The most popular search method is called matched filter or template matching, which looks for signals that have known waveforms, i. e., from well-modelled events. Using the frequency domain, the matching consists of correlating the data with a bank of waveforms created with different physical parameters through analytical and numerical methods (templates). For each template $h(t)$ and for the time series of a single detector $d(t)$ this method calculates the square of the matched-filter SNR defined by (ABBOTT et al., 2016a):

$$\rho^2(t) = \frac{1}{\langle h|h \rangle} |\langle d|h \rangle (t)|^2, \quad (3.6)$$

where the correlation is defined by:

$$\langle d|h \rangle (t) = 4 \int_0^\infty \frac{\tilde{d}(f)\tilde{h}^*(f)}{S_n(f)} e^{2\pi i f t} df, \quad (3.7)$$

which is normalized by the $\langle h|h \rangle$ factor, defined by:

$$\langle h|h \rangle = 4 \int_0^\infty \frac{\tilde{h}(f)\tilde{h}^*(f)}{S_n(f)} df. \quad (3.8)$$

Are called triggers the results of the correlation of the data with the templates that exceed a pre-established value of SNR matched-filter. The triggers generated in each detector are analyzed within a time coincidence window between the data of the detectors network, determined by the maximum possible arrival time of the supposed gravitational wave signal between them (few ms). Furthermore, triggers pass to other statistical tests to characterize consistency with a gravitational wave signal and mitigate the possibility of being caused by noise transients (ABBOTT et al., 2020a). This was the primary method to identify all gravitational wave events cataloged so far since the compact binary coalescence event is a very well modeled phenomenon.

Un-modeled (or weakly modeled) gravitational searches mostly analyze the correlated excess power of the data from different detectors represented in the time-frequency plane, rather than depending on features of an expected waveform.

3.3 Coherent analysis

When we do not have prior information about a waveform, as in searching for burst signals, an alternative is to analyze the coherence of the signals combined simultaneously from multiple detectors. The incoherent analysis individually generates the candidate events for each detector, while the coherent approach generates a unique list of candidates combining data from at least two detectors. Assuming comparable detectors, such as LIGO-Virgo, this is a natural analysis since the gravitational wave will similarly interact with them. This consideration is dependent on network angular sensitivity, which is comprised of the individual response of the detectors to the passage of a gravitational wave. Each detector response depends on the orientation between propagating the wave direction (sky source location) and the interferometers' arms arrangement. Therefore, the angular sensitivity of the detector network is related to the contribution of each detector antenna pattern (SCHUTZ, 2011).

A detector network allows obtaining more information about gravitational-wave features since it is impossible to correlate information about the data for a detector alone. With the information from two networked detectors, it is possible to distinguish the two independent polarizations $+$ and \times . Besides, it is feasible to roughly delimit a region of the sky for the GW signal source by the arrival time-delays information between the detectors. Three detectors can delimit a region of the sky with greater precision via triangulation (PANKOW et al., 2018).

Within the coherent analysis perspective, it is easier to distinguish coincidences between signals caused by a "real" gravitational wave from those caused by glitches, since the detectors' noise in the great majority are not correlated between the far detectors. The analysis is usually done with the representation of data in the time-frequency domain, allowed by wavelet transforms (KLIMENKO; MITSELMAKHER, 2004). The wavelet transform represents a time series on a specific basis, just like the Fourier transform, but in this case, the data is represented as "pixels" in time (x-axis) and frequency (y-axis). On the time-frequency domain, the power of each pixel is expressed with colors. In this way, a gravitational wave signal would cause more power in a pixel than one expects from detector noise alone, maintaining its information in time and frequency that is used in the correlation with the data of the other detectors in the network.

The triggers are selected for the set of correlated pixels that have excess power related to the noise. To evaluate the possibility of the trigger was accidentally caused by an unknown transient noise (non-gaussian) in the detector network, the false alarm rate is determined from a background estimation. For this, the data must go through a procedure that erases the possibility of detecting a "real" gravitational wave signal in a coherent analysis. The data stream of the detectors is shifted by a higher time than the time coincidence window. Within a defined time shift, the coincidence triggers are then interpreted as a background noise sample. This procedure is repeated for different time shifts, and when combined, they produce a more significant statistical background sample. Thus, each trigger selected in the coherent analysis is subjected to a false alarm rate given by the number of background triggers with equal or greater excess power (or detection statistic) divided by the total time searched for time-shifted coincidence (ABBOTT et al., 2020a). This will be discussed with more details in Section 4.4.

3.3.1 The coherent WaveBurst pipeline

The coherent Waveburst is an open-source software for gravitational-wave data analysis. From the strain data of the detector network, the cWB search pipeline uses the coherent analysis artifacts previously described to identify and reconstruct transient signals of gravitational waves without prior knowledge of signal morphology. With the computational core developed in the *C++* programming language, the cWB is one of the main pipelines used by the LIGO-Virgo-Kagra (LVK) Scientific Collaboration, working on low-latency during the observational runs and in the offline searches. Due to the good results, it is the only pipeline sensitive to generic morphologies coming from all-sky used in gravitational-wave transient catalogs. Unlike other coherent analysis approaches, the cWB uses a method that combines the individual data streams of a multi-detector network in a statistic denominated as maximum likelihood analysis that allows reconstructing the source sky location and the signal waveform. Here we present some highlights of the cWB features. A more detailed description can be found at [Klimenko et al. \(2016\)](#).

First, the data of all detectors undergo removal of persistent spectral lines (see Figure 3.4). Then the data are represented in the time-frequency domain by Wilson-Daubachies-Meyer (WDM) wavelet transform that represents the data through different bases and resolutions, allowing that data are represented with good localization properties in the time-frequency plane defined here by the parameter M ([Necula et al., 2012](#)). Thus, we can denote the WDM transform data for the k -th detector in the multi-detector network by $w_k(t, f; M)$.

The data of the entire detector network is defined in vectors with the form $\mathbf{w}_{\theta, \phi}[p] \equiv \{w_k(t - \tau_k(\theta, \phi), f; M) / \sqrt{S_k(f)}\}_{k=1..K}$ where $\sqrt{S_k(f)}$ is the noise power spectrum from the k -th detector and the short notation p represent the time, frequency and resolution coordinates. The dependency on sky coordinates θ, ϕ is necessary to compensate for the time-delay generated by the light travel of GW coming from the sources located in (θ, ϕ) when reaching the different ground-based detectors.

The energy of each pixel is maximized for the sky coordinates in the form $E_{\theta, \phi}[p] = \|\mathbf{w}_{\theta, \phi}[p]\|_2^2$ and the set of pixels that exceeds a pre-established value of energy are selected and clustered with pixels from their neighborhood, as shown in Figure 3.7 for the GW150914 signal.

Some clustering rules can promote specific geometries in the time-frequency plane. For example, the chirp aspect of typical CBC events is a preferred form in a cluster

of pixels selection. It is possible to apply other clustering rules and relaxing selection parameters in case of observation from another astrophysical source.

Based on the Time-Frequency clusters, the burst event detection parameters (signal waveform, polarization and sky location) are extracted by the likelihood method, defined as the "inverse problem". Formally, by the likelihood ratio, it is possible to assess the goodness of fit parameters of two competing statistical models. In our case, the ratio of the probability that a GW signal is present on the data and the probability of data containing only noise.

Under the assumption of Gaussian white noise, the clusters of selected pixels are evaluated by the cWB with logarithmic value of the likelihood ratio with the functional form $L_{\theta,\phi} = 2(\mathbf{w}|\xi) - (\xi|\xi)$ where ξ is the noise-scaled network response vector (KLLMENKO et al., 2016), i. e., the antenna pattern matrix which elements are scaled by $\sqrt{S_k(f)}$ to the response of GW signal $h_{+,\times}$. This vector is explicitly represented by $\xi_k[p] = [F_{k,+}h_+(t, f; M) + F_{k,\times}h_\times(t, f; M)]/\sqrt{S_k(f)}$ where $F_{k,+}(\theta, \phi)$ and $F_{k,\times}(\theta, \phi)$ are the antenna pattern function for the two independent polarizations of the k -th detector. The maximum likelihood ratio statistic is obtained by maximizing $h_{+,\times}$, as follows:

$$L_{max}(\theta, \phi) = \sum_{p \in C} \mathbf{w}_{\theta,\phi}[p]^T \mathbf{P}_{\theta,\phi}[p] \mathbf{w}_{\theta,\phi}[p], \quad (3.9)$$

where the letter C means the selected cluster of pixels, and this statistic is used to designate a significant cluster as an event candidate or trigger (GAYATHRI et al., 2019). The L_{max} statistic can be divided into two parts considering the diagonal and off-diagonal terms of the network projection operator $\mathbf{P}_{\theta,\phi}[p]$, respectively called incoherent (E_i) and coherent (E_c) energies.

The projector matrix $\mathbf{P}[p]$ is constructed over the components of the unit vectors $\mathbf{e}_+[p]$ and $\mathbf{e}_\times[p]$ in the form:

$$\mathbf{P}_{nm}[p] = \mathbf{e}_{n+}[p]\mathbf{e}_{m+}[p] + \mathbf{e}_{n\times}[p]\mathbf{e}_{m\times}[p]. \quad (3.10)$$

The null energy or residual noise energy (E_n), is estimated once the reconstructed signal is subtracted from the data, that is, $E_n = \sum_{p \in C} E[p] - L_{max}$. It provides a statistical able to quantify a cluster of pixels taken from data with large noise

excursions and, in this sense, could indicate a trigger caused by glitches.

The coherent energy (E_c) is a significant element, as its statistics depend on the cross-correlation terms in different detectors. Together, these energy statistics are used to establish essential parameters to feature the extracted triggers by the pipeline. One of them is the network correlation coefficient c_c , an efficient parameter to distinguish genuine GW signals from those caused by accidental coincident noises in the detectors. It is quantified by:

$$c_c \equiv \frac{E_c}{|E_c| + E_n}, \quad (3.11)$$

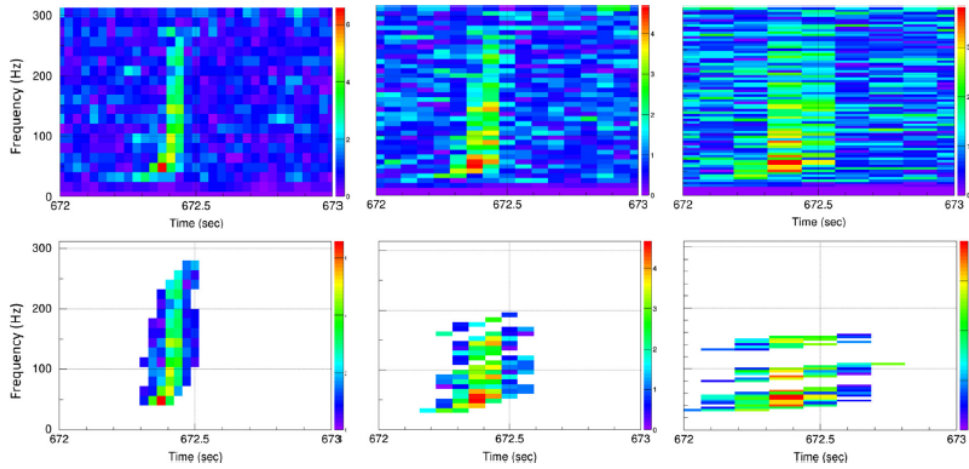
where GW signals are expected to have $c_c \approx 1$ and coincident glitches $c_c \ll 1$. The main burst detection statistic used by cWB is:

$$\eta_c = \sqrt{\frac{c_c E_c K}{K - 1}}. \quad (3.12)$$

Using K as the total number of detectors used in the cWB analysis, this equation gives us a parameter equivalent to the coherent network signal-to-noise ratio (SNR).

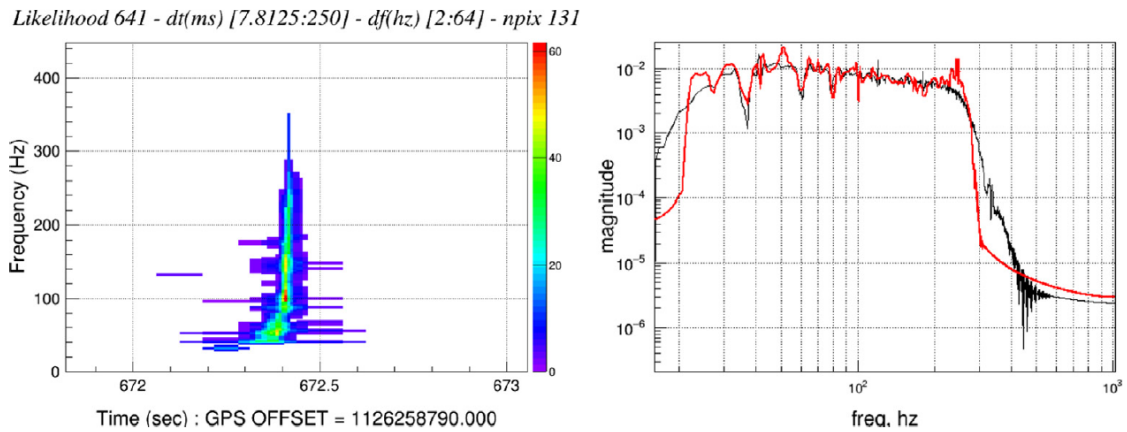
Figure 3.8 shows the reconstruction of the GW150914 signal in the time-frequency plane from the LIGO data. The details of the clustering, sky location, and detection parameters can be shown on the Coherent Event Display (CED) web page for the reconstructed and selected events.

Figure 3.7 - The selection of pixels that have excess power from the LIGO-Hanford data of GW150914. Each column is in a different resolution in the time-frequency representation.



SOURCE: Drago et al. (2021).

Figure 3.8 - On the left is the waveform reconstruction in the time-frequency plane of the GW150914 event after maximizing the likelihood. The cWB reconstruction of GW150914 in the frequency domain (red line) from a posterior signal sample (black line) is on the right.



SOURCE: Drago et al. (2021).

4 ALL-SKY SEARCH FOR GRAVITATIONAL-WAVE BURSTS AT THE SCHENBERG BAND

4.1 Motivation

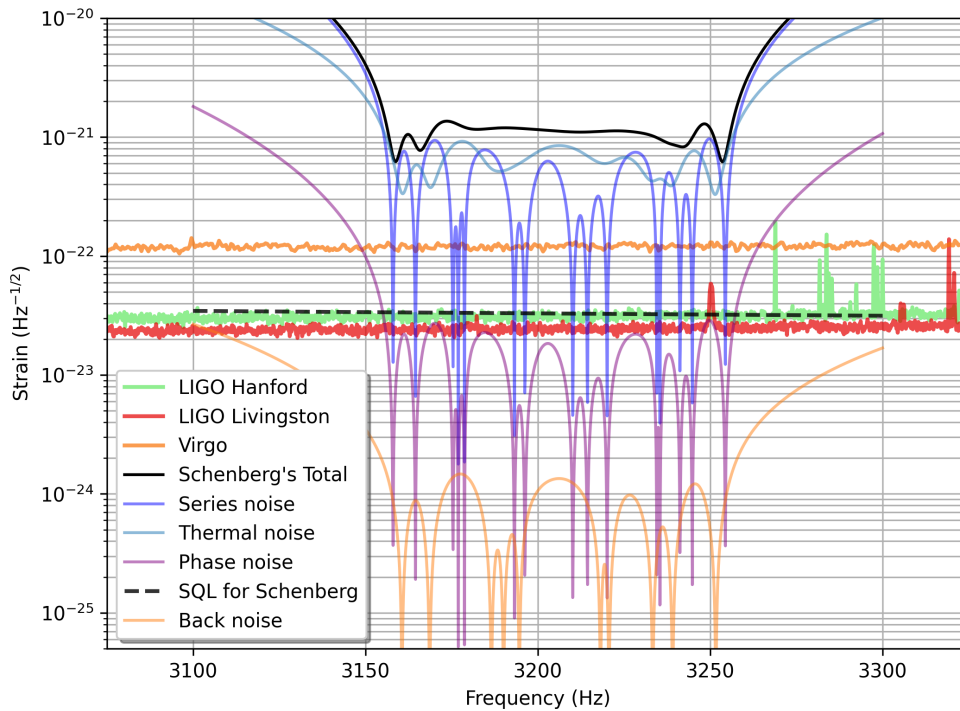
The Schenberg spherical antenna performed its last observational run in 2015 at 5.0 K with sensitivity around $\sim 10^{-20}$ Hz^{-1/2} when it was dismantled in 2016 at the University of São Paulo (OLIVEIRA; AGUIAR, 2016). However, this last sensitivity is even far from his design sensitivity at this initial version of Schenberg (iSchenberg). A higher sensitivity could be achieved by improving the electronics, the vibrational isolation and enhancing the electrical and mechanical quality factors, constructing a chamber capable of reaching high vacuum while providing interfacing with the cryogenics; ways of acquiring and processing data; and so forth (REIS, 2021). Figure 4.1 shows that the Schenberg sensitivity curve for the initial version of Schenberg (with the present electronics available in the project) is not as good as the O3 aLIGOs sensitivity curves, however supposing an advanced version of Schenberg (aSchenberg) with state of art electronics and outstanding mechanical and electric quality factors (Qs), in such a way that the series (electronic) and thermal noises would be substantially decreased, the Schenberg sensitivity would approach the standard quantum limit (flat spectrum, represented by the dashed black line). However, this "ultimate" Schenberg sensitivity is already achieved in O3 by the two LIGO interferometers, so analyzing the LIGO O3 data in the Schenberg bandwidth of sensitivity is an excellent measure to evaluate what are the chances of gravitational wave detection by an aSchenberg with "ultimate" sensitivity.

Identifying significant signals from these data may provide further motivations for the reassembly of Schenberg. Within an optimistic perspective, the Schenberg running at "ultimate" sensitivity may allow the detecting GW by another physical principle of detection, i. e., the detection by a resonant-mass antenna. The convergence of detection evidence with a ground-based interferometer would take gravitational-wave astronomy to even greater scientific consistency and foster unthinkable insights into it. Although this narrow frequency range is considerably distant from the specific region of all CBC signals detected by LIGO-Virgo so far, other events in the universe can generate signals within this band, such as described in the Subsection 3.1.1.

Therefore, our work aims to verify the recent possibility of the Schenberg spherical antenna detecting some gravitational-wave signal considering its "ultimate" sensitivity in the frequency band [3150-3260] Hz. Underpinned by Figure 4.1 and using the

coherent WaveBurst pipeline, we will search for GW burst signals in the O3 data, carried from April 1st, 2019, to March 27th, 2020. For a future scenario, it is possible to add the resonant mass detectors data into the interferometers network to be analyzed by the cWB. Signals with different characteristics demand specific searches methods. To cover a more significant number of signal morphologies and increase the chance of detection, we will carry out an all-sky search for GW bursts without previous knowledge of any waveform, so it is not proposed for specific target sources. As a matter of fact, the analysis of the results needs to be carried out carefully as identifying a significant candidate of GW at this frequency band would outstandingly impact several areas of physics and astronomy. Having this perspective in mind, we follow a well-established methodology in searching for burst signals (ABADIE et al., 2012; ABBOTT et al., 2017a; ABBOTT et al., 2019a; DRAGO, 2010; ABBOTT et al., 2005; ABADIE et al., 2010), especially the most recent search for gravitational-wave bursts in the LIGO and Virgo data (ABBOTT et al., 2021b).

Figure 4.1 - The Schenberg design strain sensitivity for the overall system (not only a single mode channel), with a non-degenerate sphere, in a cryogenic system at 0.1 K compared to the representative spectral strain sensitivity of the LIGO Hanford (29 April 2019 11:47 UTC), LIGO Livingston (5 September 2019 20:53 UTC) and Virgo (10 April 2019 00:34 UTC) during O3. The Schenberg sensitivity curve for the initial version of Schenberg (with the present electronics available in the project) is not as good as the O3 aLIGOs sensitivity curves, however supposing an advanced version of Schenberg (aSchenberg) with state of art electronics and outstanding mechanical and electric Qs, in such a way that the series (electronic) and thermal noises would be substantially decreased, the Schenberg sensitivity would approach the standard quantum limit (flat spectrum, represented by the dashed black line). However, this "ultimate" Schenberg sensitivity is already achieved in O3 by the two LIGO interferometers, so analyzing the LIGO O3 data in the Schenberg bandwidth of sensitivity is an excellent measure to evaluate what are the chances of gravitational wave detection by an aSchenberg with "ultimate" sensitivity. The detector model used to construct the Schenberg sensitivity curve is not yet published.



SOURCE: Own authorship.

4.2 The search configuration

Due to the extensive amount of data, we used the cWB allocated to a LIGO cluster settled at the California Institute of Technology, whose certification is managed by the LIGO Data Grid (LDG), and communication with the cluster is established via Secure Shell Protocol (SSH). The LDG is responsible for connecting the LIGO Scientific Collaboration (LSC) computational and data storage resources into a grid computing software.

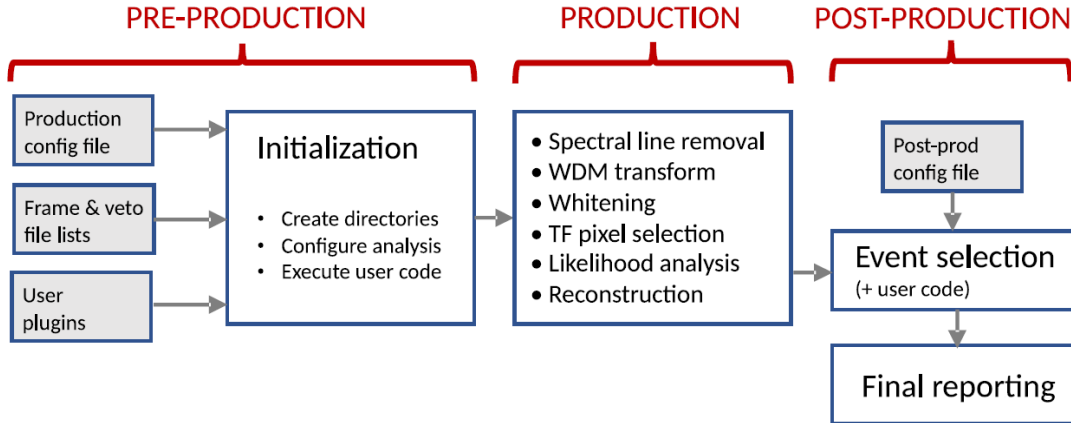
The pipeline configuration is set via file inputs written in *C++* programming language. Examples and parameter explanations can be found in the cWB documentation, available at [Klimenko et al. \(2022\)](#). Figure 4.2 shows the functional diagram of the cWB pipeline, which is divided into three main stages: pre-production, production, and post-production. The cWB-6.4.1 version was used in this work ([KLIMENKO et al., 2021](#)).

The pre-production step is dedicated to setting up the primary directory that receives all the scripts and files necessary to run the pipeline analysis. The production configuration file contains the main search setup as the origin of the strain data paths, the analyzed frequency bounds, parameters thresholds to select triggers, whitening and wavelet parameters, and more. The cWB has default values for the most part of the parameters. A further step is to include a data quality file list that comprises all data quality flags, used to identify and veto triggers caused by noise, and remove poor quality data segments. The user plugins files customize the software without changing its source code. The simulation study, described in Section 4.5.1, is configured in those files.

The main part of the analysis has been commented on previously, in Subsection 3.3.1 and summarize the production stage. At this point occur the extraction of potential triggers according to the parameters established in the pre-production stage. The total observation data is broken into small segments to be analyzed separately to optimize computational efforts, called jobs.

In the post-production stage, we set further thresholds in the population of output triggers from the production stage, to select significant candidate events. It displays text files with reconstructed parameters and figures of merit for a list of survived triggers from the parameters thresholds in a web page report.

Figure 4.2 - Functional diagram showing the main stages of the cWB pipeline.



SOURCE: Drago et al. (2021)

4.3 Data set

The data from the Third Observational Run (O3) were collected from April 1, 2019, to March 27, 2020, and included the two LIGO detectors and Virgo’s participation. From October 1, 2019, to November 1, 2019, a commissioning break split O3 into two large parts, the first one containing six months of data (O3a) and the second part known as O3b, which all together corresponds to 330 days of observational run. The analysis presented here is based on both parts of the O3 data set.

The coherent analysis of the data requires the participation of more than one detector. Especially for high frequencies, Virgo had a considerably higher noise floor than the LIGO detectors for O3. Therefore, Virgo’s participation in the coherent analysis does not improve the selection of coincident events, while the high rate of non-Gaussian noise would increase the overall false candidates. In order to maximize the chance of detecting real GW events, we use only the Hanford-Livingston (HL) network. This path agrees with other works on coherent search for unmodeled signals in O3 (ABBOTT et al., 2021b; ABBOTT et al., 2021a).

During the O3a run, the duty cycle, i.e., the amount of time in the run that the instruments were effectively observing, were 71% (130.3 days) for LIGO Hanford and 76% (138.5 days) for LIGO Livingston. For O3b, the duty cycles were 79% (115.7 days) for LIGO Hanford and 79% (115.5 days) for LIGO Livingston (DAVIS et al., 2021b). All the GW strain O3 data used in this work are available at the Gravitational Wave Open Science Center (GWOSC) sourced from the channel *DCS-*

CALIB_STRAIN_CLEANSUB60HZ_C01 and can be found at [LIGO Scientific Collaboration And Virgo Collaboration \(2020\)](#).

The amount of analyzed data is reduced due to the requirement of coincident observation of the HL network and the removal of poor quality segments of each detector's data stream, a total of 102.5 days of data for O3a and 93.4 days for O3b.

In addition to the background noise, which forms the stationary spectrum, detectors are affected by several sources of transient noise that interferes with the data quality. When identifying noise sources it is possible to differ transients caused by noise from those caused by gravitational waves, thus reducing the number of false alarms. With that purpose, many sensors and auxiliary channels monitor the detectors and their surroundings during the entire data acquisition time. When an excessive noise is recorded and an auxiliary channel has identified its source, the respective time in the detector's strain data is labeled as likely to contain instrumental artifacts using a data quality flag to indicate, with different categories, the state of the detector and the analyzed data ([DAVIS et al., 2021b](#)). The list of data quality vetoes with the fraction of removed data and their respective noise sources for O3 that was considered in this work is available at [Davis et al. \(2021a\)](#).

The Advanced LIGO data is calibrated to detect frequencies from 10 Hz to 5 kHz. Frequencies outside this bandwidth do not have neither uncertainty characterization and an assigned reliability. Some works characterized the calibration uncertainty of the data during O3a ([SUN et al., 2020](#)) and O3b ([SUN et al., 2021](#)). However, they are characterized only in the 20-2000 Hz frequency band and do not comprise most of the frequency range analyzed here.

Despite that, the LIGO-Virgo-Kagra Scientific Collaboration (LVK) makes the LIGO and Virgo calibration uncertain to public access at GWOSC with all observational runs. It can be accessed at [LVK \(2021\)](#).

Using the files of calibration error and uncertainty estimated for LIGO, we characterize the frequency range of 512-4096 Hz given at different epochs, which is displayed on [Table 4.1](#). Therefore, it is possible to establish values corresponding to the 68% limits and the median value for phase and magnitude errors of the data. The maximum median values represent the best estimates of the systematic error bounds. More details about this issue, the calibration model and the methodology can be found at [Sun et al. \(2020\)](#).

Table 4.1 - O3 calibration epochs, the maximum 1σ , median excursions of response from unity magnitude and zero phases in the frequency band 512–4096 Hz.

Hanford epoch	Max 1σ magnitude [%]	Max 1σ phase [deg]	Max median magnitude [%]	Max median phase [deg]
Mar 28–Jun 11	16.75	9.68	1.21	1.36
Jun 11–Aug 28	5.70	2.65	1.90	0.54
Aug 28–Oct 1	7.62	3.67	2.66	0.89
Nov 1–Jan 14	5.92	2.65	1.79	0.58
Jan 14–Feb 11	5.64	2.57	2.11	0.62
Feb 11–Mar 16	5.64	2.57	2.11	0.62
Mar 16–Mar 27	11.80	11.52	2.00	6.66
Livingston epoch	Max 1σ magnitude [%]	Max 1σ phase [deg]	Max median magnitude [%]	Max median phase [deg]
Mar 28–Jun 11	9.24	5.98	2.15	2.16
Jun 11–Oct 1	4.64	4.99	2.17	3.26
Nov 1–Jan 14	7.05	3.36	3.16	0.86
Jan 14–Mar 27	6.74	3.22	3.60	1.15

The upper limit on systematic error and the associated uncertainty of LIGO detectors in O3 are $<17\%$ in magnitude, <12 deg in phase, and <1 μ s in timing for O3. Also, according to Sun et al. (2020) the estimation of the network timing uncertainty is around 10 microseconds, so it is negligible compared to the uncertainty in estimates of the time-of-arrival for any GW event (~ 1 millisecond). Furthermore, these fluctuations of amplitude calibration are not expected to significantly impact the search presented here. However, they can affect the estimation of the efficiency and upper limits, which will be discussed later (ABBOTT et al., 2021b).

4.4 Analysis procedure

The primary approach of our analysis is based on the production step outputs of cWB from the all-sky search for short gravitational-wave bursts in O3 strain data (ABBOTT et al., 2021b). Using the high-frequency analysis of this work, which covers the frequency band 512–4096 Hz, we set up the post-processing of cWB to select triggers that either have an estimated central or have part of the bandwidth overlap with the Schenberg band. In this last case, we consider signals with more energy outside the 3150–3260 Hz band but still have detectable energy in the band of interest.

For each trigger generated in the search, the cWB establishes a tree of parameters, containing different information reconstructed from the power excess identified in the coherent data, such as bandwidth, central frequency, duration, network correlation coefficient, coherent network SNR, and others. There are also information about parameters for each detector.

The candidate events are selected in the post-production stage by setting thresh-

olds on trigger parameters. The data has been reduced from 16384 Hz to 8192 Hz to optimize computational costs. This new sampling rate defines the maximum frequency analyzed (4096 Hz) according to the Nyquist–Shannon sampling theorem (BRACEWELL, 2000) and defines the resolution of the time delay filters.

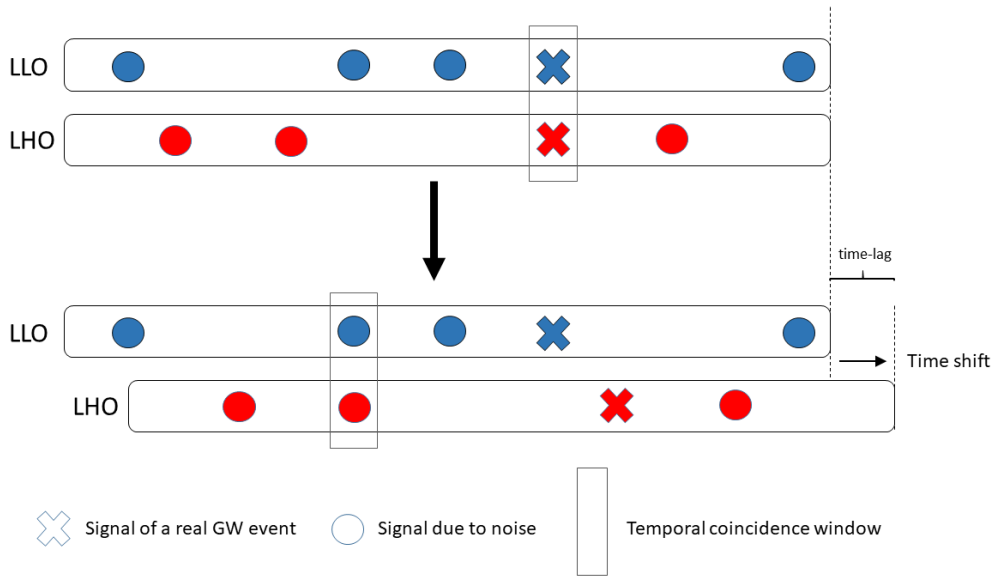
The search in Abbott et al. (2021b) differs from the one presented here in both post-production thresholds and its efficiency characterization. Although the same triggers generated by another search are used here, there are no expectations of getting the same statistical significance results. The assess of the significance of the coincident events are changed when selecting candidates from different thresholds. It is due to the background triggers analysis, which uses the same thresholds on the post-production stage, which is different from the mentioned paper. So, a different background sample set will generate a particular zero-lag statistics significance.

At the end of the search, it will be possible to establish some astrophysical interpretations of the results even in the null detection possibility. It can be performed by characterizing the sensitivity of the search. In this procedure, simulated GW signals (injections) are added on the HL data stream, and the pipeline is engaged to detect them considering the same configuration of the main search (ABBOTT et al., 2019a). More details are displayed in the Section 4.5.

4.4.1 Background analysis

It is necessary to know the statistical properties of transient accidentals due to noise (defined here as background triggers) to evaluate the significance of a burst candidate event. The time shift procedure creates these background samples. As mentioned before, it consists of shifting the data stream of one detector concerning the other by a time interval more extensive than the coincidence window of the search for triggers in a livetime T_{bkg} . The triggers generated by a coherent search in this time-lag are fortuitous and they are interpreted as a background sample since a GW burst signal cannot cause them, as exemplified in Figure 4.3. Repeating this procedure for several time-lags brings a more robust background estimate. However, performing this procedure with an indefinite number of time shifts does not result in a better background estimates as it saturates as a function of time-shifts number (WAS et al., 2010).

Figure 4.3 - Schematic representation of the time shift procedure for background estimation. The zero-lag (not shifted stream) coincidence situation between the LIGO Livingston (LLO) and Hanford (LHO) detector data is illustrated at the top. In this case, a GW signal, represented by the symbol X, can be found within the time coincidence window, i. e., a few ms. At the bottom, the LHO data stream temporally shifted when compared to the LLO data. In this time-lag configuration, the signal due to excess power of the noise (represented here by circles) and within the coincidence time window is described as a background trigger.



SOURCE: Adapted from Davis (2020).

The background estimate was also based on the O3 all-sky short burst search outputs. The set of background triggers was selected in the post-production stage using the same thresholds in the parameters of the zero-lag search triggers. With noise samples characterized in this way, it is possible to assess the significance of zero-lag events by comparing the detection characteristics between both populations. Therefore, we select the triggers with the central frequency or part of the bandwidth overlapped with the Schenberg band. The trigger bandwidth was defined from the maximum and minimum frequency parameters associated with the time-frequency map pixels. A network correlation coefficient threshold $c_c = 0.8$ is used in our analysis.

The time distribution of background events suggested that it was necessary to divide the O3a analysis into chunks of consecutive time epochs, defined as “chunks”. Chunk

1 runs from the beginning of O3 until May 16, 2019, and has the event population at higher detection statistics than the rest of O3a, defined as chunk 2. This issue remains even after applying the data quality cuts, suggesting a period with more significant influence of noise in the high-frequency band. It happens in the epoch with the highest value of the magnitude calibration uncertainties of both LIGO detectors, as it is shown in Table 4.1. The uncertainties found for the value of the strain amplitude in the data for this period indicates a more significant fluctuation in the maximum amplitude, which is related to higher statistical detection triggers due to the considerable excess power of the noise described by the background evaluation. The O3b epoch is all covered in chunk 3. Therefore, the analysis of O3 is then divided into these three temporally separated large blocks of data.

The background was estimated with a lag size of 1199 seconds with 1 second of lag step for all the chunks, i. e., the data stream of one detector is shifted 1200 times, each one in a particular amount of analyzed time-lag T . The cWB incorporates the application of super lags to improve the background statistics. We can understand super lags by visualizing the data from the detectors illustrated in Figure 4.3 as part of a single data segment. The super lag is a significant delay in the detectors time that performs a mix of different segments, in which the data are shifted 1200 times for each new super lag configuration. The O3a chunks had five super lags, while the O3b chunk had two super lags. With these features, the background livetime of O3 was estimated to be over 1100 years, and the total livetime for the individual chunks is explicit in Table 4.2.

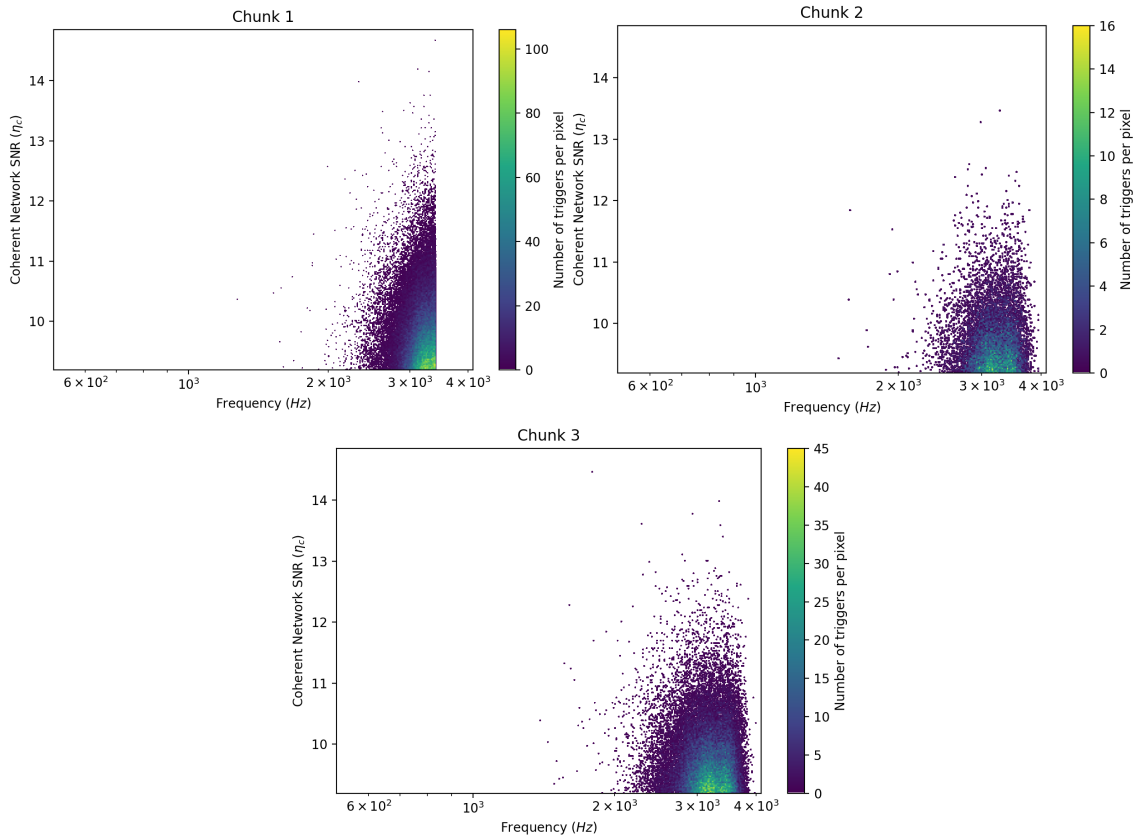
Table 4.2 - Background livetime for the different epochs of O3.

Chunk	Livetime (years)
1 (O3a)	296.2
2 (O3a)	258.3
3 (O3b)	569.5

After applying the post-production triggers thresholds and the vetoes, the cWB is able to create a report in the form of a web page, which comprises the main results of the background analysis in text and image file formats, in which the formation of the results are configured in the post-production file.

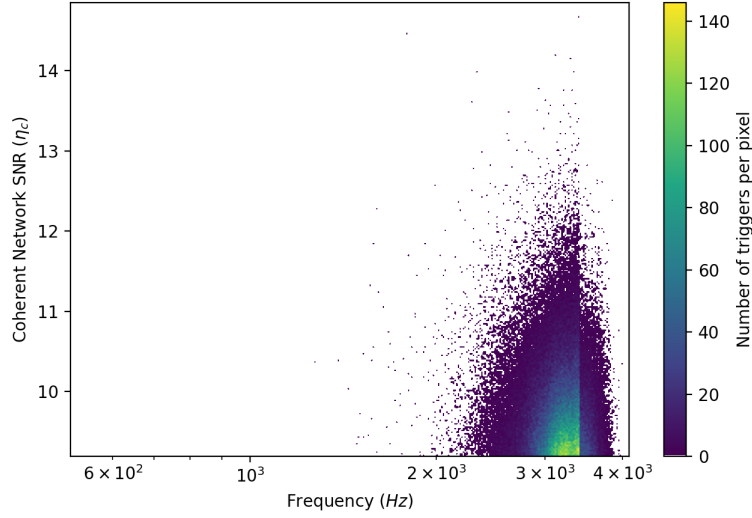
We also added a frequency cut discarding triggers with central frequencies (f_0) above 3400 Hz and below 896 Hz for the first chunk. This additional threshold was necessary as the coherent network SNR distribution of the triggers strongly depended on the central frequency for those with $f_0 > 3400$. Also, two triggers with $\eta_c > 41$ were identified as outliers as they significantly diverged from the rest of the population of background triggers and had $f_0 \sim 800$ Hz. The thresholds on the previously mentioned frequency parameters remain valid for the rest of the chunks. The frequency dependence of the background triggers for each data chunk can be seen in Figure 4.4. Note that a significant population of triggers occupies the lowest coherent network SNR values.

Figure 4.4 - The magnitude distribution of coherent background triggers, characterized by the coherent network SNR plotted versus the central frequency values. It is possible to see more significant triggers about the other data chunks from the beginning of the first half of O3 until May 16, 2019 (chunk 1). The loudest ones grows as the frequency increases and justify the cut produced at $f_0 > 3400$ in order to obtain a cleaner distribution.



SOURCE: Own authorship.

Figure 4.5 - The magnitude distribution of all coherent background triggers in O3.



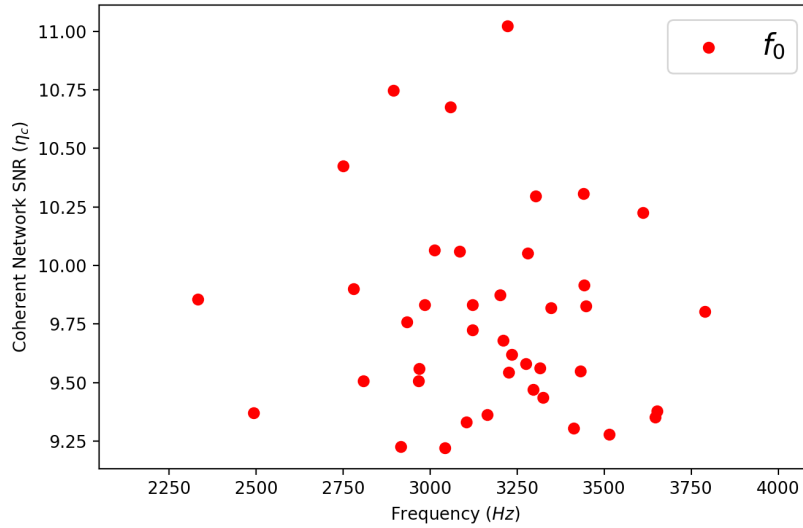
SOURCE: Own authorship.

4.4.2 Zero-lag analysis

The significant zero-lag coincident triggers are short-duration transients that are candidates for gravitational-wave burst events. They were selected using the same thresholds parameters triggers of the background evaluation, that is, triggers coincident with $c_c \geq 0.8$ and f_0 or part of bandwidth within 3150–3260 Hz were selected, except for chunk 1, which also had a frequency cut discarding central frequencies $896 \geq f_0$ and $f_0 \leq 3400$. The zero-lag livetime of the first half of O3 was 21.7 days for Chunk 1, 80.8 days for Chunk 2, and the second half of O3 was 93.4 days.

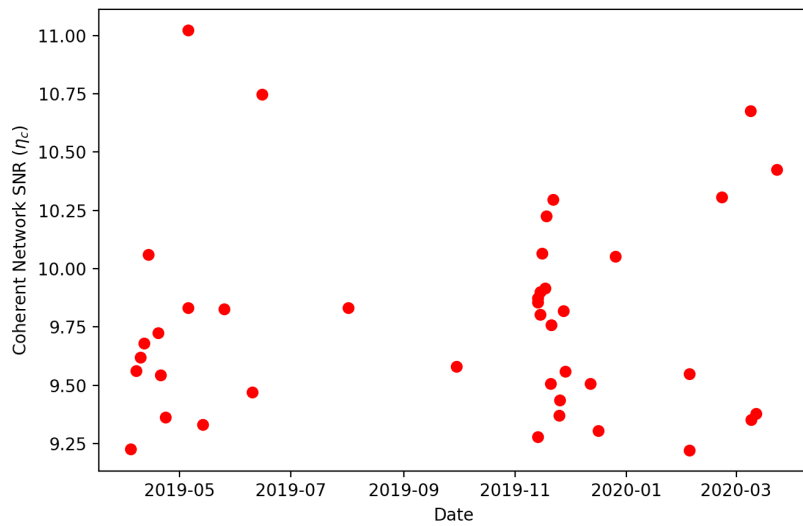
Forty-one not vetoed cWB triggers have survived the post-production thresholds, of which sixteen were identified in the O3a epoch and twenty-five in O3b. We can observe the distribution of η_c as a function of the candidate events central frequency and the date that they were detected all over the O3 livetime in Figures 4.6 and 4.7, respectively. The loudest event has a central frequency at 3222 Hz, $\eta_c = 11.0$, and occurred on May 05, 2019, epoch corresponding to chunk 1.

Figure 4.6 - The distribution of zero-lag triggers burst detection statistic, characterized by the coherent network SNR, as a function of the reconstruct central frequency values. Most of the population of identified events has a central frequency outside the Schenberg band.



SOURCE: Own authorship.

Figure 4.7 - The time distribution of candidate events over the entire O3 livetime with the respective values of η_c .



SOURCE: Own authorship.

4.4.3 Detection statistics

To assess the significance of the candidate events described by Figure 4.6, it is necessary to ponder them by some detection statistics. In this way, we can distinguish triggers generated by a GW signal from those caused by transient noise more appropriately. The type of detection statistic frequently used in the gravitational-wave research field is the False Alarm Rate (FAR). The FAR is a statistic assigned to each zero-lag trigger (now sometimes referred to foreground triggers) when a background trigger population is characterized and ranked by an intermediate detection statistic. In cWB, the ranking statistic is performed by the coherent network SNR, the higher η_c the stronger is the coherent signal compared to the noise and the more likely it is to be detected. We calculate the FAR by counting the total number of time-shifted triggers with η_c greater than the zero-lag trigger in question and dividing it by the total amount of background triggers search time (lives in Table 4.2). Therefore, the smaller the FAR value of an event, the less likely it is caused by the detector's noise. For each candidate event, the FAR is calculated using the equation:

$$FAR = \frac{N}{\sum_i T_i}, \quad (4.1)$$

where N is the total number of background triggers with an intermediate statistic greater or equal than the candidate in question and T_i is the amount of analyzed time in background trial i (KEPPEL, 2009). Note that different background features in its estimation, including distinct thresholds and trigger rates, will lead to different statistical significance for the foreground triggers. Therefore, this procedure is done for the different chunks separately before obtaining a joint analysis.

The so-called Inverse False Alarm Rate (IFAR) is a common way of representing this quantity and is calculated by just taking the inverse of the FAR amount previously estimated. Operating the Equation 4.1 and knowing in advance the FAR value of a candidate, the expected number of triggers below this value due to the background is then $FAR \times T_0$, where T_0 is the zero-lag livetime.

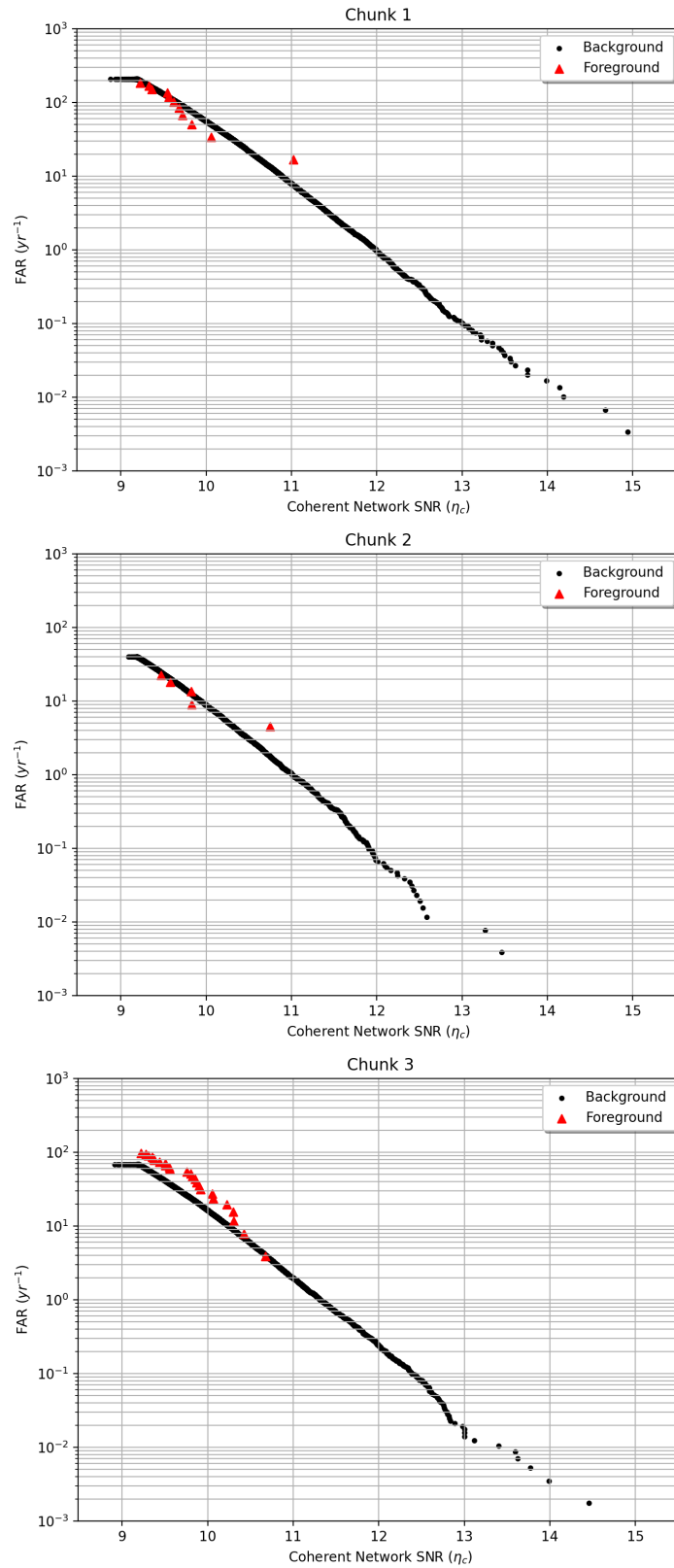
4.4.3.1 Significance of candidate events

One way to compare the behavior of triggers during the zero-lag and background trials is to analyze the FAR distribution as a function of η_c . The FAR of each population (foreground and background) in this frame is calculated separately, i.e., dividing

the number of triggers with a value of η_c greater or equal than the trigger in question by search livetime of each population. Therefore, when calculating FAR as follows (sometimes seen as cumulative FAR), we examine a rate at which events more significant than the corresponding detection statistic occurs (ABBOTT et al., 2017a). Identifying the zero-lag search results as background distribution outliers may indicate burst signals candidates. We can see in Figure 4.8 this type of evaluation taken individually for three chunks of data.

Although some candidate events does not precisely follow the background distribution, none differ notably from what would expect for a significant GWs event. The low number of samples of zero-lag triggers might be responsible for the slight discrepancy to the population of background triggers which was estimated with a large number of samples due to the background livetime T_{bkg} . We can look at the significance of events from a more quantitative perspective and increase the relevance of our analysis.

Figure 4.8 - The FAR versus ranking statistic η_c for all observation periods of O3: chunk 1 (top), chunk 2 (middle), and chunk 3 (bottom).

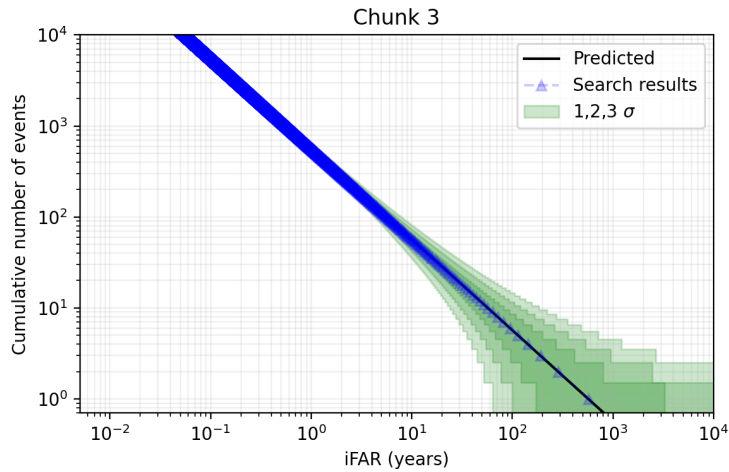


SOURCE: Own authorship.

4.4.3.2 Expected and observed results

Accidental coincidences like background triggers are independent random events and experimentally follow a Poisson distribution. Guide by the False Alarm Rate, we can assign a significant analysis of the zero-lag coincident events within a Poisson confidence interval of the expected values of the background. In this context, if the candidate events are caused by independent random noise, they will have the same significance within a statistic window concerning the background. One form to represent this type of analysis is by the cumulative number of triggers as a function of IFAR. According to Equation 4.1, and now writing it another way, for each trigger, the expected number of background events louder than this one is then $\Sigma_i T_i / \text{IFAR}$. If we are only evaluating the background triggers found in the T_{bkg} livetime, they must fall exactly into the expected distribution of the background, as it can be seen in Figure 4.9.

Figure 4.9 - The cumulative number of background triggers versus IFAR for O3b. Since we are looking at the background triggers represented by the blue triangles, they should fall precisely on the expected line of the background. The green area shows the one, two, and three-standard deviation errors on the expected value of the background estimate, assuming a Poisson distribution.



SOURCE: Own authorship.

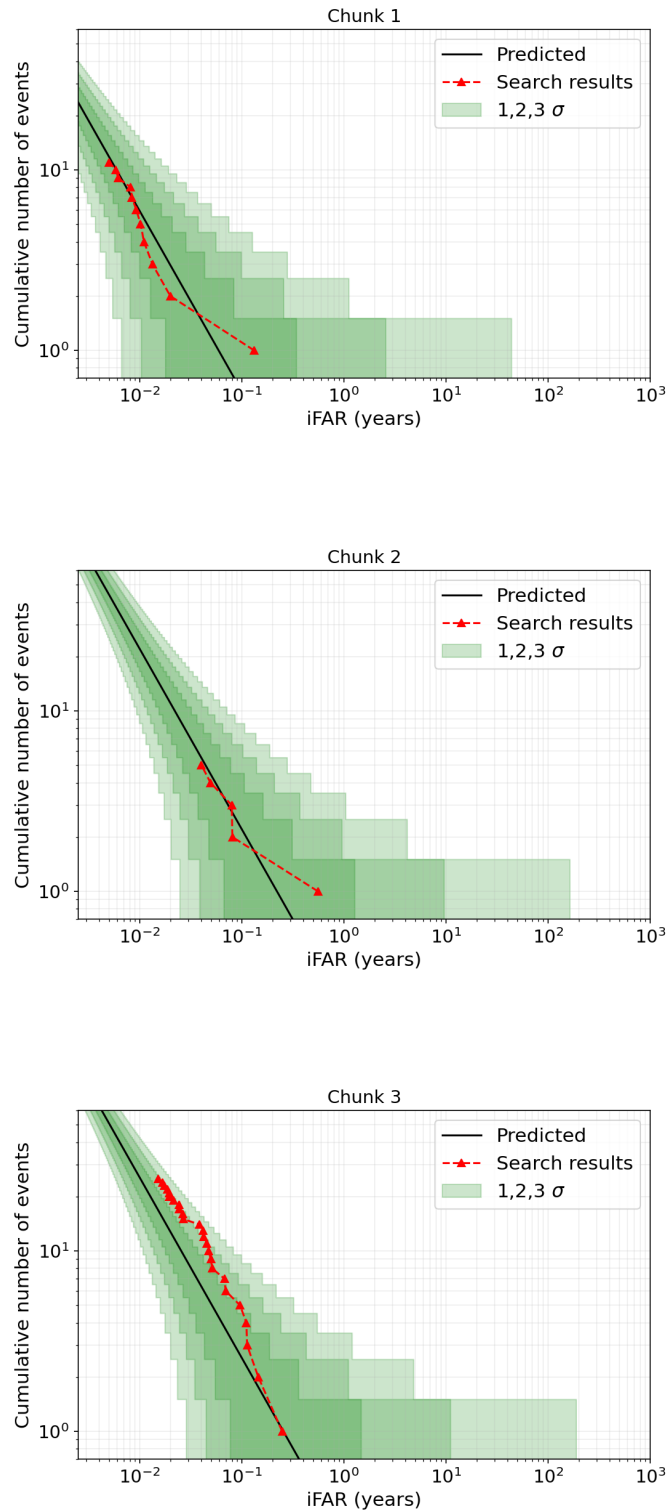
Therefore, considerable deviations (more remarkable than the Poisson uncertainty regions) in the IFAR values evidence a burst detection candidate. We set an IFAR threshold of 100 years to identify a significant detection according to other searches

for gravitational-wave bursts (ABBOTT et al., 2017a; ABBOTT et al., 2019a; ABBOTT et al., 2021b).

Finally, using the definition of Equation 4.1, we calculate the IFAR for the candidate events of each chunk and plot the cumulative number of coincident zero-lag events against the expected number of triggers above the particular IFAR due to background, calculated by T_0/IFAR . The results can be seen in Figure 4.10.

The loudest event of this analysis ($\eta_c = 11.0$) has an IFAR of 0.1 years. However, the most significant candidate belongs to chunk 2 and obtained an IFAR of 0.6 years despite having $\eta_c = 10.7$. This is because chunk 1 has more background triggers with great coherent network SNR compared to chunk 2, as you can see in Figure 4.4. Thus, despite the loudest, it does not differ considerably from the expected value due to the background.

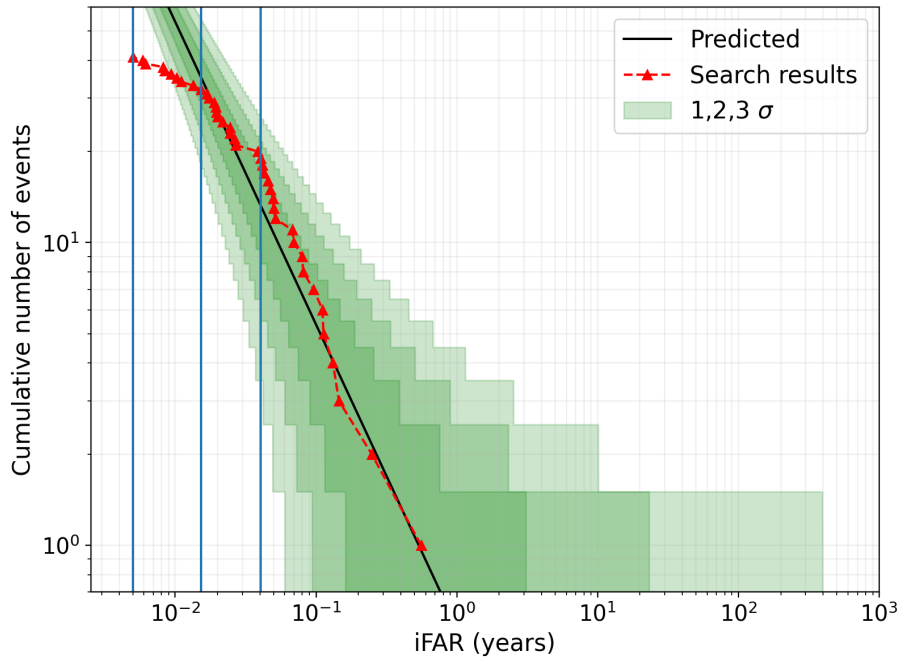
Figure 4.10 - The cumulative number of events above a threshold IFAR, for zero-lag coincident events, shown as red triangles. The expected background (given the analysis time by definition) is shown as a solid black line.



SOURCE: Own authorship.

The joint analysis results of all O3 can be obtained by combining the significance of the zero-lag triggers estimated separately, and the expected values are estimated by all O3 livetime, as shown in Figure 4.11.

Figure 4.11 - The cumulative number of zero-lag triggers versus IFAR for all O3. The vertical blue lines represent the minimum IFAR values for each chunk and the positions of the kinks.



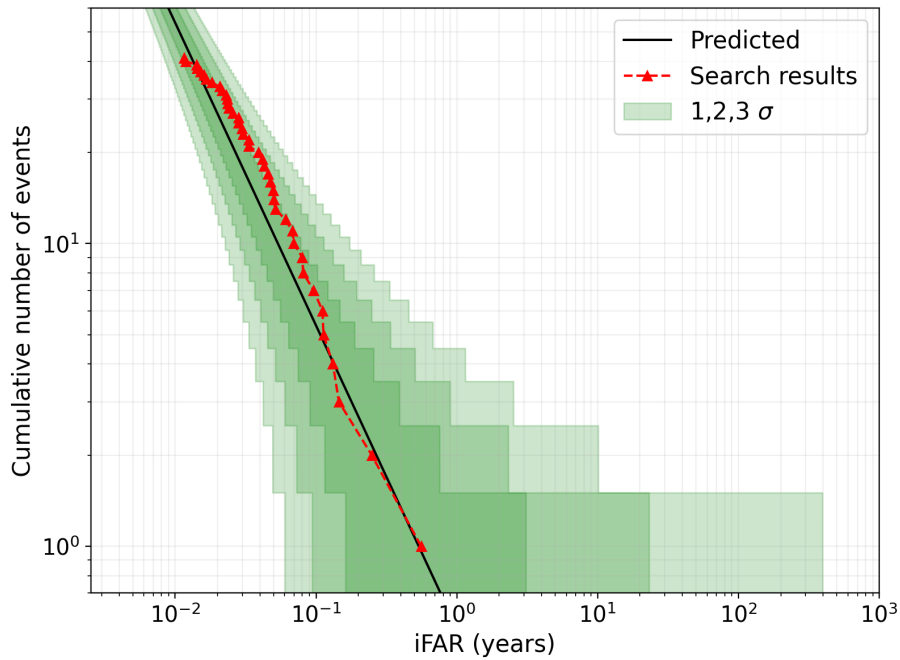
SOURCE: Own authorship.

Note that the cumulative number of detected events is lower than the expected number due to the background for less significant triggers. There is a kink whenever you reach for a minimum IFAR value of each chunk. That does not mean that we obtained a smaller population of zero-lag triggers than was expected by the background, as the results suggest. In fact, it happens when combining different categories of triggers, delimited here by the different chunks. This effect occurs because when each minimum IFAR is reached, one less category is left to be combined. A discussion of this effect can be seen in [Keppel \(2009\)](#). The best thing to do in this situation is to normalize the FAR by the number of categories remaining rather than the total, via the equation:

$$FARc = \frac{1}{m} \left\{ \left[\sum_{j=1}^m \Theta(FAR_{max,j} - FAR) \right] \times FAR + \sum_{j=1}^m [\Theta(FAR - FAR_{max,j}) FAR_{max,j}] \right\}, \quad (4.2)$$

where m is the number of categories (three in our case) and $\Theta(x)$ is the Heaviside function. Using the combined False Alarm Rate, we can represent more rigorously the results of the significance of zero-lag triggers over the entire O3 livetime as shown in Figure 4.12.

Figure 4.12 - The cumulative number of zero-lag triggers versus the combined IFAR for all O3 after normalization.



SOURCE: Own authorship.

None of the events reached a sufficient significance to be considered a likely gravitational-wave event, and they are all compatible with the background in three-sigma, in conformity with [Abbott et al. \(2021b\)](#).

4.4.3.3 False alarm probability analysis

An alternative way to evaluate the significance of a gravitational-wave candidate event is by the False Alarm Probability (FAP), which starts with the previously hypothesis: the triggers generated by noise follow a Poisson distribution. The FAP estimates the probability that one of these backgrounds triggers with the same statistical ranking (or louder) as a gravitational-wave candidate will occur at least once in the search period T_0 (ZHENG et al., 2021) and is calculated by:

$$FAP = 1 - e^{-N(T_0/T_{bkg})}. \quad (4.3)$$

Therefore, the probability of getting any background triggers louder than the loudest zero-lag trigger is 36.2%. The null result in the chunks agrees with the expected false alarm probability for a significant event considering all O3, i. e., an event with FAR ≥ 100 years would have a FAP of $\leq 0.5\%$. The FAP was computed for the forty-one zero-lag triggers, and it can be seen systematically in the Tables A.1, A.2 and A.3 of the Appendix.

4.5 Astrophysical interpretation of the results

4.5.1 Search sensitivity

With the end of the search, it is possible to establish some astrophysical interpretations of the results, even not identifying signals with sufficient statistical significance to characterize a detection of gravitational-wave bursts. We evaluated the efficiency of reconstructing burst signals by the cWB using the Monte Carlo method. In this procedure, simulated GW signals are added ("injected") on the LIGO data stream, and the cWB pipeline is engaged to detect them considering the exact configuration of the zero-lag search. These are software (*ad hoc*) injections that simulate gravitational-wave bursts' passage through the LIGO detector network. The cWB contains the MDC Engine, a built-in generator of burst waveforms that provides options to specify waveforms, sky distribution, polarization, injection rate or time, and amplitude of the injections. The details of the procedure sketch and how to generate MDC injections for simulation studies with the cWB are available at Klimentko et al. (2020).

The signal strength of the injections is usually expressed by the components of the signal polarizations, in the form of root-sum-squared strain amplitude (h_{rss}):

$$h_{rss} = \sqrt{\int_{-\infty}^{\infty} (h_+^2(t) + h_\times^2(t)) dt}, \quad (4.4)$$

and is interpreted as the amplitude of the GW that reaches Earth, i.e., previous to reduction by the detector antenna pattern (MARKOWITZ et al., 2008). The h_{rss} has units of $\text{Hz}^{-1/2}$, which allows a direct comparison with the spectral strain sensitivity of the detectors. Some strain factors are used to rescale the defined amplitude for every simulated signal injected, improving the estimate efficiency statistic.

Despite not being derived from any specific astrophysical model, the *ad hoc* waveforms can approximate the morphology of different GWs sources. So, it was necessary to organize and produce a set of appropriate simulated signals.

Mainly motivated by expected sources for gravitational-wave bursts on the Schenberg band (as described in Section 3.1.1), we defined a set of fourteen injections composed by two waveforms. Those are Sine-Gaussians (SG) and Ring-Downs (RD) signals, both circularly polarized with central frequency within [3150 Hz – 3260 Hz]. The parameterization of the waveform is represent as the following:

$$\begin{bmatrix} h_+(t) \\ h_\times(t) \end{bmatrix} = A \times \begin{bmatrix} \frac{1+\alpha^2}{2} \\ \alpha \end{bmatrix} \times \begin{bmatrix} H_+(t) \\ H_\times(t) \end{bmatrix}, \quad (4.5)$$

where A is the strain amplitude, $H_{\times/+}(t)$ are the waveforms for the two independent polarization and $\alpha = 1$ for the circular polarization, which assumes an optimally oriented source and is the best case scenario (ABADIE et al., 2012). The sky location of the injected waveforms presents an isotropic distribution. In our simulation analysis, we used nine strain factors over a grid of h_{rss} ranging of $5.00 \times 10^{-23} \text{ Hz}^{-1/2}$ to $4.05 \times 10^{-21} \text{ Hz}^{-1/2}$ with logarithmically spaced values stepping of $\sqrt{3}$.

To characterize the search sensitivity by the simulation procedure it is necessary to set up the analysis on the pre-production stage. We organized the important files as follows: the production config file and the plug-in where the injection parameters are defined.

4.5.1.1 *Ad hoc* waveforms set

The decaying sinusoid waveform is characterized by the dumping time τ , the central frequency value f_0 , and polarization. Therefore, the waveform for the two independent polarizations can be parameterized as:

$$\begin{aligned} H_+(t) &= \exp(-t/\tau)\sin(2\pi f_0 t), \\ H_\times(t) &= \exp(-t/\tau)\cos(2\pi f_0 t). \end{aligned} \tag{4.6}$$

These Ring-Down waveforms represent the population of short burst GWs due to nonradial quasi-normal excitation modes in Neutron Stars, especially the fundamental modes (f-modes) associated with a pulsar glitch or a magnetar flare (GLAMPEDAKIS; GUALTIERI, 2018). Soft Equations of State (EoS) enables f-modes emission at frequencies up to around 3 kHz and a typical damping time of 100 ms (ANDERSSON; KOKKOTAS, 1998). The post-merger neutron star (PMNS), the scenario of forming a massive and differentially rotating neutron star, are also sources with this signal morphology. In the situation where PMNS survives prompt-collapse, non-axisymmetric deformations occurs in the NS remnant that generates short GW bursts (~ 10 – 100 ms) whose waveform resembles Ring-down with dominant oscillation frequency ~ 2 – 4 kHz associated with quadrupole oscillations in the fluid (CLARK et al., 2014). Based on these features, we injected Ring-Downs with damping time τ of 5 ms, 50 ms, and 100 ms with the frequency centered in the Schenberg band (3205 Hz). Furthermore, there are two other injections with $\tau = 100$ ms with a defined central frequency on the edge of the Schenberg band, 3150 Hz and 3260 Hz.

As a convention, we will adopt the following terminology for Ring-Down injections: **RDC f_0 " τ "damping_time**, where C represents the circular polarization, f_0 is the injected central frequency value, and the number after τ indicates the value of damping time in milliseconds. Therefore, the RDC3205 τ 100 injection indicates a Ring-Down waveform with circular polarization, $f_0 = 3205$ Hz and $\tau = 100$ ms.

Sine-Gaussian waveforms are sine waves modulated by a Gaussian envelope and are characterized by polarization, central frequency, and the ratio of central frequency to bandwidth, known as quality factor parameter Q. The Sine-Gaussian injections are used because they cover a great range of burst parameters space by changing the value of Q and are parameterized by:

$$\begin{aligned}
H_+(t) &= \exp\left(-\frac{2t\pi^2 f_0^2}{Q^2}\right) \sin(2\pi f_0 t), \\
H_\times(t) &= \exp\left(-\frac{2t\pi^2 f_0^2}{Q^2}\right) \cos(2\pi f_0 t).
\end{aligned}
\tag{4.7}$$

We produced injections with three different quality factor values, 3, 9, and 100, each with three central frequencies representing the beginning, middle and end of the Schenberg band. Following the convention, Sine-Gaussian waveforms are named by their parameters under the form **SGC** f_0 **"Q"****quality_factor**. Therefore, the SGC3150Q9 injection has a circular polarization, a central frequency of 3150 Hz and Q=9. Tables 4.3 and 4.4 systematically presents the set of injections inserted in the simulation study.

Table 4.3 - Set of Sine-Gaussian waveforms injections.

Sine-Gaussian wavelets (circular)		
SGC3150Q3	SGC3150Q9	SGC3150Q100
SGC3194Q3	SGC3205Q9	SGC3194Q100
SGC3260Q3	SGC3260Q9	SGC3260Q100

Table 4.4 - Set of Ring-Down waveforms injections.

Ring-Down damped oscillation (circular)				
RDC3150 τ 100	RDC3205 τ 100	RDC3260 τ 100	RDC3205 τ 050	RDC3205 τ 005

4.5.1.2 Efficiency analysis

There are no previous work in the literature that has injected signals into the data of the third Advanced LIGO run with a central frequency in the band examined here. Thus, there is a need to characterize the search sensitivity for burst signals by studying its efficiency to evaluate the possibility of detection of the Schenberg antenna.

The search efficiency is estimated by evaluating the cWB’s capability to detect and reconstruct the injected signals for different amplitude grid values. It is susceptible to some factors such as the features of the waveforms, the injected central frequency, cWB configuration and mostly by the thresholds in the post-production stage. Therefore, varying any of these parameters will generate different results.

For the efficiency analysis, we use all cWB work stages. After setting the initial cWB configuration for injections in the pre-production and the analysis ran in the production step, the results were collected in the post-production stage. The injections were subjected to the same post-production thresholds of the foreground and background study to create the efficiency estimation. In this work, we only selected triggers with bandwidth within the Schenberg frequency band and with network correlation coefficient $c_c \geq 0.8$.

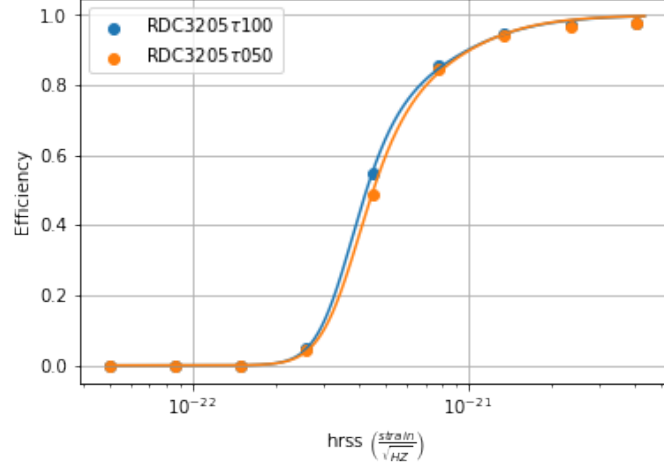
Furthermore, we selected only the injections with the criterium for a significant detection, i.e., with IFAR ≥ 100 years. The FAR distribution over the coherent Network SNR resulted by the background estimation (Figure 4.8) was used to provide the IFAR cut for each one of the chunks. Therefore, a detected injection with η_c equivalent to an FAR ≥ 0.01 years⁻¹ is discarded in the search efficiency estimation. The threshold of the parameters are related as follows: the c_c threshold implies minimum values of η_c (since they have a direct proportionality) that produces the estimation of the background significance distribution. So, for each injection with some η_c value, we guarantee the target FAR threshold.

Therefore, the search efficiency analysis is produced considering the number of a hypothetical source population (*ad hoc* waveforms) that survive to the post-production thresholds without regard to the events’ origin (sky location), and it is quantified by the fraction of injections that the pipeline can have detected among them.

The detection efficiency can be appropriately represented as a function of the strain amplitude grid since a more significant number of detected events is expected for those with greater h_{rss} . The choice of the scaling factor amplitude was stipulated to obtain an efficiency curve that covers from 0% to close to 100% detection efficiency as illustrated by Figure 4.13. By fitting the efficiency curve, we obtain the values of h_{rss} that achieves 10%, 50%, and 90% detection efficiency for each injection and use these indicators to study and compare the different waveforms and searches. To fit, the cWB uses two complementary error functions ($\text{erfc}(x) = 1 - \text{erf}(x)$) where the junction between them should be at h_{rss} with 50% efficiency. Table 4.5 explicitly displays the value of h_{rss} for these detection efficiency ratios, where we can explore

astrophysical consequences by relating it to the waveform’s astrophysical motivation, for example.

Figure 4.13 - Representative plot of the efficiency curve for two Ring-Down injections in O3a epoch.



SOURCE: Own authorship.

Table 4.5 - Values of h_{rss} in units of $10^{-22} \text{ Hz}^{-1/2}$ for 10%, 50% and 90% detection efficiency in O3a and O3b at the chosen FAR threshold of 1/100 years.

Morphology	$h_{rss}^{10\%}$		$h_{rss}^{50\%}$		$h_{rss}^{90\%}$	
	O3a	O3b	O3a	O3b	O3a	O3b
Ring-Down damped oscillation (circular)						
RDC3205τ005	3.0	3.2	4.8	4.8	12.5	10.3
RDC3205τ050	2.9	3.1	4.5	4.7	9.7	9.3
RDC3150τ100	2.8	3.0	4.3	4.4	9.4	9.0
RDC3205τ100	2.9	3.1	4.4	4.5	9.6	9.2
RDC3260τ100	3.0	3.2	4.8	4.9	10.3	9.8
Sine-Gaussian wavelets (circular)						
SGC3150Q3	3.3	3.5	5.6	5.4	20.6	17.3
SGC3194Q3	3.4	3.4	5.6	5.2	28.7	14.5
SGC3260Q3	3.6	3.6	5.9	5.4	37.9	15.2
SGC3150Q9	3.0	3.2	4.9	4.8	15.3	10.8
SGC3205Q9	3.1	3.2	5.0	4.9	14.0	11.2
SGC3260Q9	3.2	3.3	5.2	5.0	16.3	12.3
SGC3150Q100	2.7	2.9	4.3	4.5	9.5	9.0
SGC3194Q100	2.7	2.9	4.3	4.5	8.5	8.9
SGC3260Q100	3.0	3.2	4.5	4.9	9.5	9.3

According to Table 4.5, the h_{rss} values obtained for different efficiency rates are consistent when comparing O3a and O3b, giving no significant deviations. It is important to highlight that for the same injected central frequency, the detection efficiency by the cWB is better for the waveforms with better-characterized narrow band morphologies in the frequency domain, namely, the Sine-Gaussians with high-Q and Ring-Downs with high- τ .

Take note that estimated values of h_{rss} from the efficiency study are susceptible to the sensitivity fluctuations on the LIGO detectors in the frequency band considered here, and has its uncertainties featured by the calibration errors in Table 4.1, for the respective epochs.

4.5.2 Detection range

The relation established between the amplitude of the *ad hoc* waveforms and the detection efficiency allows the study of astrophysical implications. A comprehensive way of representing the search sensitivity characterization is by expressing the previous results from amplitude to the emitted energy as gravitational waves by potential astrophysical sources. To obtain this association, we start from the flux of a gravitational-wave burst in the Fourier domain developed through the energy-momentum tensor of GWs, and is given by (SUTTON, 2013):

$$F_{GW} = \frac{\pi c^3}{4G} \frac{1}{T} \int_{-\infty}^{\infty} f^2 (|\tilde{h}_+(f)|^2 + |\tilde{h}_\times(f)|^2) df, \quad (4.8)$$

where T is the total burst duration. Since the GW flux quantity represents the radiated energy per unit area per unit time, when integrating it over a sphere surrounding the source with a radius r (distance to the source) and duration T , the equation below gives the total energy isotropic emitted:

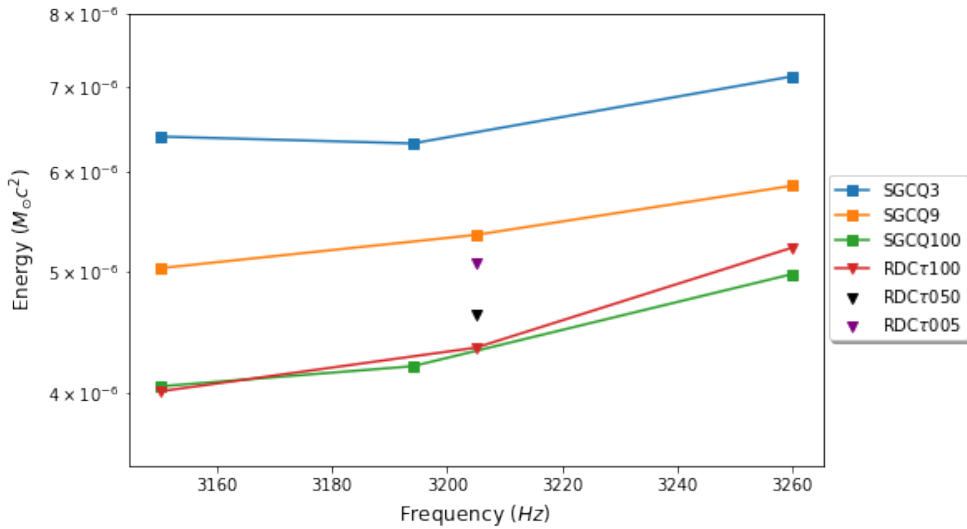
$$E_{GW} = \frac{\pi^2 c^3}{G} r^2 \int_{-\infty}^{\infty} f^2 (|\tilde{h}_+(f)|^2 + |\tilde{h}_\times(f)|^2) df. \quad (4.9)$$

In the adopted emission pattern scheme, if we assume that the *ad hoc* waveforms are narrowband with central frequency f_0 , the integrand that remains is the root-sum-squared strain amplitude in the frequency space and is connected to Equation 4.4 by Parseval's theorem (BRACEWELL, 2000), resulting in:

$$E_{GW}^{iso} = \frac{\pi^2 c^3}{G} f_0^2 r^2 h_{rss}^2. \quad (4.10)$$

This equation is valid for injections circularly polarized. Assuming a standard-candle burst source at a distance of $r_0 = 10$ kpc, we obtain the expected emitted energy for signals with the injections morphologies. Figure 4.14 shows these energy values as a function of the injections central frequency for O3, obtained from the mean values of $h_{rss}^{50\%}$ among O3a and O3b.

Figure 4.14 - The GW-burst emitted energy expressed in units of solar masses which correspond to 50% detection efficiency at an IFAR ≥ 100 years, for standard-candle sources emitting at 10 kpc for the waveforms listed in Table 4.5 into the Schenberg band. It is expected that the behavior of the RDC τ 050 and RDC τ 005 waveforms will follow the same frequency dependence as RDC τ 100.

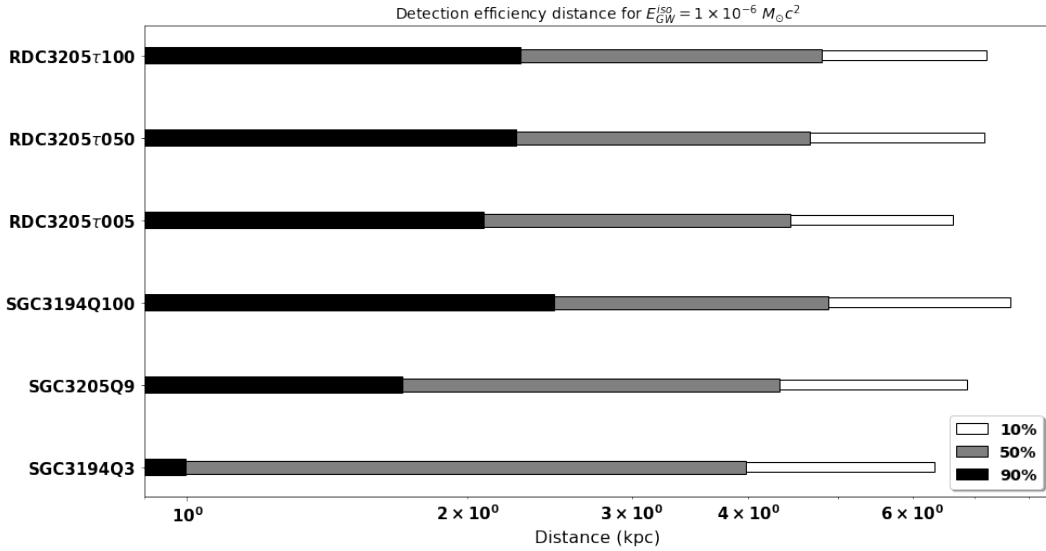


SOURCE: Own authorship.

In other words, by connecting the h_{rss} with a specific efficiency value from our simulation study, Equation 4.10 quantifies the minimum amount of energy that needs to be (isotropically) radiated by the GW source in order to be detected by cWB. The progressive increase of the energy in the Figure 4.14 is a consequence of the noise spectral amplitude dependence with the frequency increases, which results in recovered injections with greater amplitudes considering the band [3150-3260] Hz in the LIGO detectors.

When solving the Equation 4.10 for the distance r and fixing a GW energy value, we get another perspective on the detection range. With this scenario, the detection efficiencies obtained can be used to evaluate the approximate range to detectable sources (the radius of a sphere centered on the source) of a gravitational-wave burst with isotropic emission. The Figure 4.15 shows the distance range for 10%, 50% and 90% of detection efficiency expressed as overlapping bars for the fixed energy $E_{GW}^{iso} = 1 \times 10^{-6} M_{\odot}c^2$. When setting other values to the emitted energy we obtain the equivalent detection distance range, with a scale of $\sqrt{E_{GW}^{iso}}$.

Figure 4.15 - The minimum distance, in kiloparsecs (kpc), for the waveforms listed in Table 4.5, for detection efficiencies of 10%, 50% and 90% at an IFAR ≥ 100 years and $E_{GW}^{iso} = 1 \times 10^{-6} M_{\odot}c^2$.



SOURCE: Own authorship.

4.5.3 Upper limits

Other astrophysical interpretations emerge from the detection efficiency results in the absence of a coherent event with sufficient significance to indicate a detection. It is evident that we need a greater rate of astrophysical events producing signals reaching the Earth with low strain amplitudes in order to achieve a sufficient probability of detection. Thus, some of these events could be detected even if the $h_{r_{SS}}$ are linked to low detection efficiency. On the other hand, events with greater strain amplitude have higher detection efficiency and are more likely to be detected. Therefore they do not require to hit the Earth at a greater rate. Regarding this framework,

we can set an upper limit in the burst source population rate by recalling the Poisson distribution of potential astrophysical sources, i. e., the measure of a number of random independent events and uncorrelated in the livetime T .

Considering the mean rate R of foreground events (which follow the Poisson distribution), the detection efficiency ϵ of an event and the mean number b of background events in the livetime T , the probability of detecting N events in T is:

$$P(N|\epsilon\lambda + b) = \left(\frac{(\epsilon\lambda + b)^N}{N!} \right) e^{-(\epsilon\lambda + b)}, \quad (4.11)$$

where $\lambda = RT$ is the expected number of foreground events. Assuming a confidence level c and given n measured events, the frequentist upper limit λ_c at a confidence level c is the value at which there is a probability $(1 - c)$ of measuring more than n events (DRAGO, 2010), explicitied by:

$$1 - c = \sum_{N=n+1}^{\infty} P(N|\epsilon\lambda_c + b) = 1 - \sum_{N=0}^n P(N|\epsilon\lambda_c + b). \quad (4.12)$$

So, in the no detection case $n = 0$, assuming the zero background approximation $b = 0$ and 90% of confidence level ($c = 0.9$), the Equation 4.12 results in:

$$1 - 0.9 = P(0|\epsilon\lambda_{90\%}) = e^{-\epsilon\lambda_{90\%}}. \quad (4.13)$$

Finally, the 90% confidence upper limit on the total event rate $R_{90\%} = \lambda_{90\%}/T$ is:

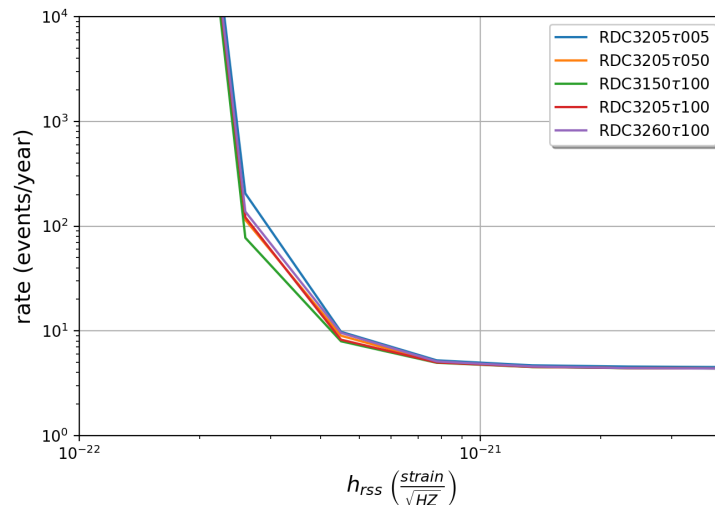
$$R_{90\%} = \frac{2.3}{\epsilon T}, \quad (4.14)$$

where $2.3 = -\ln(1 - 0.9)$. In our case, the denominator is $\sum_i \epsilon_i T_i$ where the index i indicates that the values of detection efficiencies ϵ and zero-lag livetime T corresponds to the O3a and O3b trials. More information about the mathematical description of event rate upper limits can be seen at Sutton (2009), Brady et al. (2004), Feldman and Cousins (1998). In the limit of strong signals ($\epsilon_i \approx 1$) the quantity $\sum_i \epsilon_i T_i$ goes to 195.9 days, resulting in a 90% confidence upper limit rate of 4.29 events yr^{-1} in the [3150-3160] Hz band. Thus, the resulting upper bounds are limited by the total search livetime T_0 .

Using Equation 4.14, we calculated the upper limits at 90% confidence of the rate of gravitational-wave burst for all injections set. Figures 4.16 and 4.17 show these upper limits as a function of signal strength (h_{rss}) for Ring-Down and Sine-Gaussian waveforms, respectively.

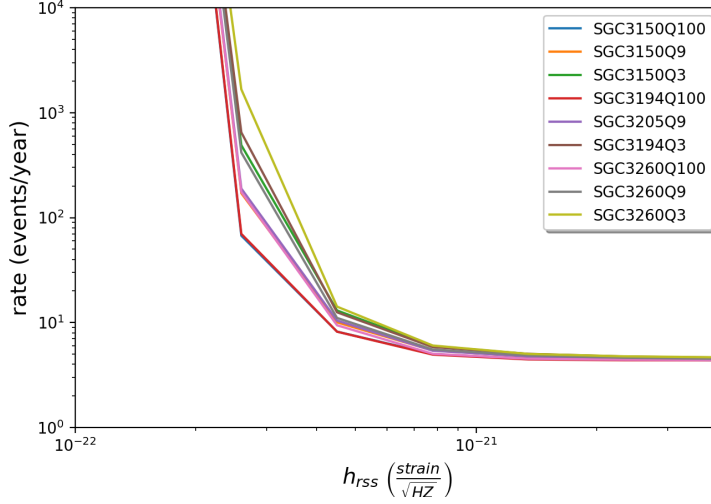
When the event rate exclusion curve is obtained as a function of the strain amplitude, it can be used in the statistics to bound the rate of GW burst events coming from a known source population and discern it to particular amplitudes. If we are looking at a well-modeled event, it is possible to accurately relate the upper limits rates to an exclusion distance range.

Figure 4.16 - Upper limits of gravitational-wave burst event rate at 90% confidence as a function of the strain amplitude h_{rss} for Ring-Down waveforms with central frequency in the Schenberg band [3150-3260] Hz. The results include both O3a and O3b epochs.



SOURCE: Own authorship.

Figure 4.17 - Upper limits of gravitational-wave burst event rate at 90% confidence as a function of the strain amplitude h_{rss} for Sine-Gaussian waveforms with central frequency in the Schenberg band [3150-3260] Hz.



SOURCE: Own authorship.

4.5.4 Detectability of f-modes

As mentioned earlier, f-modes are an effective emission medium of gravitational-wave bursts in rotating neutron stars (NS) under abrupt deformations. Depending on the EoS of the neutron star matter, the f-modes can emit GWs with frequencies that can reach the Schenberg band, although many do not achieve this frequency band. From the search sensitivity characterization results and the detection range estimation, we can assess the potential f-modes population by following a similar methodology adopted at Araujo et al. (2005). To obtain a reasonable estimate it is necessary to bring some considerations and first-order approximations, mainly because of the assumed variables' uncertainties and for being an issue that is not entirely established in general.

First, we will assume that the same mechanism as pulsars glitches generates the f-modes and that they are excited to a level that all their energy E_{GW} is supplied by the energy of the glitch E_{glitch} . In this scenario, we have a broad range of glitch energies $E_{glitch} \approx 10^{37} - 10^{47} \text{erg} \approx 10^{-17} - 10^{-10} M_{\odot} c^2$ due to the broad range of glitches size, according to Ho et al. (2020) that uses the following energy model:

$$E_{glitch} = 4\pi^2 I \nu_s \Delta\nu_s = 3.95 \times 10^{40} \text{erg} \left(\frac{\nu_s}{10 \text{Hz}} \right) \left(\frac{\Delta\nu_s}{10^{-7} \text{Hz}} \right), \quad (4.15)$$

where neutron star moment of inertia is $I \sim 10^{45} \text{gcm}^2$, ν_s is the neutron star spin, and Δ_s is the glitch size. Then we consider that the f-modes stimulated by the glitches are generated at the Schenberg frequency, i. e. in the band [3150-3260] Hz, with a typical damping time of 100 ms (ANDERSSON; KOKKOTAS, 1998). Next we can associate the expected morphology of the f-mode signals with the waveform RDC3205 τ 100, for example.

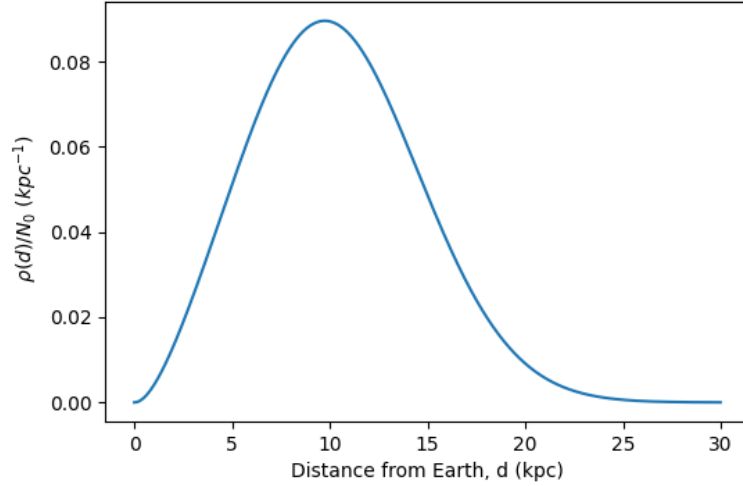
In the same way as done in Subsection 4.5.2, we can associate a detection distance range to this waveform with different levels of detection efficiency given the range of glitch energies. After everything that has been done so far, a fair question to be asked is: what is the population of f-modes at a given distance d from Earth?

As seen in Figure 4.15 and remembering the energy range of the glitches, a Galactic distance detection range is expected, and, therefore, we will turn to the spatial distribution of Galactic neutron stars to answer this question. We adopt here the recent model for Galactic neutron star population based on the star formation pattern in the Galactic disk (REED et al., 2021):

$$\rho(d) = \frac{N_0 d^2}{\sigma_r^2 z_0} \int_0^1 \exp \left[-\frac{xd}{z_0} \right] I_0 \left[\frac{R_e d \sqrt{1-x^2}}{\sigma_r} \right] \exp \left[-\frac{R_e^2 + d^2(1-x^2)}{2\sigma_r^2} \right] dx, \quad (4.16)$$

which gives the likelihood that a neutron star is a distance d from Earth, where I_0 is the modified Bessel function, $\sigma_r = 5 \text{kpc}$ is a radius parameter, N_0 is the total number of Galactic neutron stars, $z_0 = 2.0 \text{kpc}$ is the adopted disk thickness, $R_e = 8.25 \text{kpc}$ is the distance from the Galactic Center to Earth and the scaled variable x is related to the height z (cylindrical coordinates) by $x = z/d$. For further details, we suggest the reader verify Reed et al. (2021). Figure 4.18 shows the normalized probability density distribution of Galactic NS $\rho(d)/N_0$ in 30 kpc of distance from Earth.

Figure 4.18 - Normalized probability density distribution of Galactic neutron stars at 30kpc.



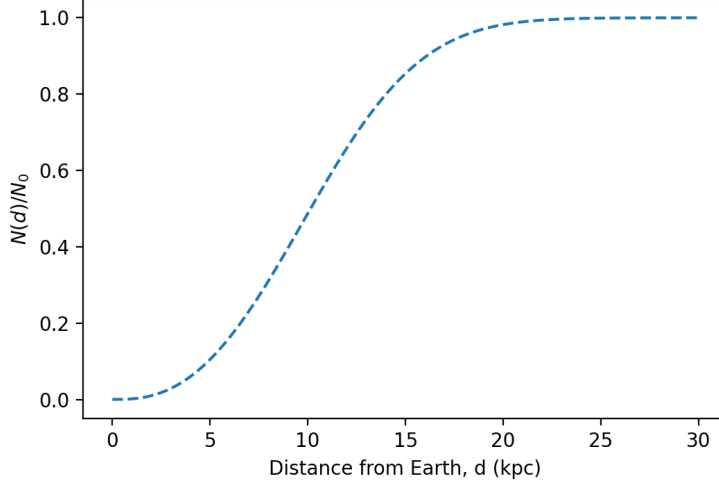
SOURCE: Own authorship.

The total number of NS at the chosen distance d may be estimated by integrating the probability density distribution $\rho(d)$, which gives the cumulative distribution function $N(d)$, defined as:

$$N(d) = \int_0^d \rho(y) dy. \quad (4.17)$$

Figure 4.19 shows the normalized cumulative distribution function of Galactic neutron stars $N(d)$ for the same 30 kpc distance from Earth.

Figure 4.19 - The normalized cumulative distribution function of Galactic neutron stars at 30kpc.



SOURCE: Own authorship.

While considering a population of f-modes signals equivalent to the injection RDC32057100, i. e., a Ring-Down waveform circularly polarized, with central frequency $f_0 = 3205\text{Hz}$, damping time $\tau = 100\text{ms}$, IFAR $\geq 100\text{ years}$ and also taking the glitch mechanism with a optimistic energy $E_{\text{glitch}} \approx 10^{-10} M_{\odot} c^2 \approx E_{\text{GW}}^{\text{iso}}$, we get the distance range at 50% efficiency detection $d^{50\%} = 0.04\text{ kpc}$.

To obtain the population of f-modes from our assumptions, it is essential to also know the glitch rate in neutron stars, which can be estimated from the observation of the known population of neutron stars, the pulsars. However, not all studied pulsars exhibit glitches. The Jodrell Bank Observatory timing program monitors 800 pulsars. It has achieved, in some cases, over 50 years of timing history on individual objects, but only 178 pulsars have at least one glitch detected. Thus we can consider that 22% of the known pulsars presents the glitch phenomenon. Some glitches are likely to be detected in the pulsars without any currently known events, so this fraction ($\sim 20\%$) should be considered a lower limit of the intrinsic fraction of glitching pulsars (BASU et al., 2022).

Different pulsars display different types of glitch behavior, including the glitch rate, the dependence on the spindown magnitude and the characteristic age of the pulsar.

Furthermore, it is difficult to characterize the glitch rate population with a single value. In [Basu et al. \(2022\)](#) the glitch rate of an individual pulsar is calculated given as constant in time and therefore should be seen as only approximations. The authors considered the average glitch rate for the entire interval in which the pulsar has been monitored for glitches and found 0.05 yr^{-1} as the median glitch rate value for 134 monitored pulsars samples.

Based on these last assumptions, and recalling the hypothesis of the f-modes is caused by pulsar glitches, we obtain a rough estimation of the f-mode events rate:

$$0.2 \times 0.05 = 0.01 \text{ events/year/pulsar.} \quad (4.18)$$

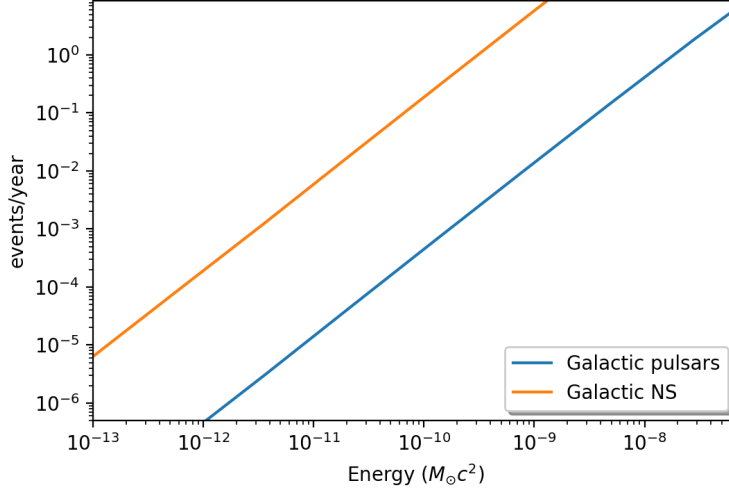
The number of pulsars in the whole Galaxy was estimated by [Yusifov and Küçük \(2004\)](#). After considering the beaming factor correction, they predicted $N_0 \sim 2.4 \times 10^5$ pulsars with luminosity greater than 0.1 mJy kpc² 1400MHz in the Galaxy. Then, by the Equation 4.17 considering $d = d^{50\%}$ and $N_0 \sim 2.4 \times 10^5$, we reach the number of potential glitching pulsars that could be seen by LIGO and Schenberg. Finally, to obtain the number of potential f-modes events per year we multiply it by the Equations 4.18, which gives:

$$5 \times 10^{-3} \text{ events/year.} \quad (4.19)$$

The detectable event rate would be significantly enhanced if all Galactic neutron stars followed the same behavior as known pulsars concerning the considered mean glitch rate and the population fraction that exhibits glitch activity. The N_0 would go to 10^{-8} ([REED et al., 2021](#)) which results in 0.19 events/year . Both values are lower than the upper limit of gravitational-wave burst event rate at 90% confidence expected for injection RDC3205 τ 100, which is around 8.7 events/year at 50% detection efficiency (see Figure 4.16).

Figure 4.20 shows the potential number of f-mode events per year versus different values of E_{glitch} considering the entire estimated Galactic population of pulsars and neutron stars at a distance $d^{50\%}$. If it is possible to characterize a family of glitches with energy E , this figure shows the respective expected f-mode event rates for the Schenberg detection.

Figure 4.20 - The number of f-mode events per year, as a function of glitch energy for the estimated population of Galactic neutrons stars and pulsars. The y-axis goes up to the upper limit value for burst rate at 50% detection efficiency (which is ~ 8.6 *events/year* according Figure 4.16), and it can be interpreted roughly here as an upper limit in the energy value of f-modes generated by NS glitches.



SOURCE: Own authorship.

In the best scenario, it would require about 5.3 years of observational search, if not more, for glitches with typical energy of $E_{glitch} = 10^{-10} M_{\odot}c^2$ to get a single f-modes detection considering the entire population of neutron stars at a certain distance $d^{50\%}$. On the other hand, it would require at least an year of observational search when considering a glitch population with twice this energy value.

The results obtained here are considerably less optimistic for the detectability of f-mode by the Schenberg spherical antenna compared to Araujo et al. (2005) which adopted signals with $SNR = 1$ and $SNR = 3$ as detection requirement. As much as we are considering an intrinsic glitch rate ~ 5 times bigger than them and also a higher strain sensitivity for the Schenberg antenna, our condition to get a detection range just for significant signals (with $IFAR \geq 100$ *years*) decreases considerably the expected event rate.

5 CONCLUSIONS

This dissertation presents an all-sky search for transient gravitational waves of short duration with minimal assumptions on the signal morphologies in the third Advanced LIGO run (O3), whose results are motivated to characterize the feasibility of burst signals detection by the Schenberg antenna. The similarity between the "ultimate" sensitivity of aSchenberg and the sensitivity of LIGO in O3 is the initial assumption of our study. Using this information, we were able to investigate the Schenberg detection potential, even though the Brazilian antenna is currently inactive. The two advanced LIGO detectors, Livingston and Hanford, were operating from early-April 2019 to late March 2020, with a greater sensitivity to GWs than any previous LIGO run. The collected O3 data were analyzed offline with the coherent WaveBurst pipeline covering frequencies from 512 Hz to 4069 Hz. The GW burst candidates were selected in the post-production stage for those with reconstructed bandwidth that overlapped the Schenberg band.

From the O3 data acquisition, a total of 195.9 days of LIGO coincidence observation time satisfied the data quality requirements so that the analysis could be performed. As demanded by the differences in the background events distribution, the data were separated into three chunks, in which no significant burst events candidates were found. The detected signals were caused by accidental coincidences according to the expected distribution for the background noise. However, this result does not suggest that the Schenberg antenna will not detect anything if reassembled with the same sensitivity at that frequency, given the random nature of events occurring in our universe. After all, for Poisson statistics, observing zero events is consistent with a non-zero event rate, as indicated in the Subsection 4.5.3.

Regarding the search sensitivity to circularly polarized waveforms at an IFAR threshold of 100 years, we defined a detection range and set upper limits on the rate of gravitational-wave bursts on Earth. We focus on two simple *ad hoc* waveform morphologies to cover the sources with emissions at 3150 Hz to 3260 Hz: Sine-Gaussians with different quality factors through the Schenberg band and Ring-Downs with specific damping times. The study of search sensitivity for simulated signals was also used to characterize the Schenberg detection range. We estimated what amount of mass converted into GW burst energy at a given distance (10 kpc) would be strong enough to be detected by the search with 50% efficiency and is around $5 \times 10^{-6} M_{\odot} c^2$. When performing the same procedure again and specifying the GW burst energy, we provide approximate estimates of the distances at which representative waveforms

could be detected with 10%, 50%, and 90% efficiency. The detection range analysis adopted isotropic emission energy to generalize the results. It is possible to associate a more precise detection distance for a well-modeled event knowing that typical GW energy is not isotropically emitted, and also the detection range can increase if we assume an optimally oriented source (regarding the line of sight).

Additionally, we set upper limits with 90% of confidence on the rate of gravitational-wave bursts at Earth. By the efficiency study, we related the upper limits to the strain amplitude (h_{rss}) of the chosen waveforms. Since the evaluation of upper limits depends on the search livetime, we better constrain the rates of GW bursts as we increase the observational run duration. That could be used to infer a more accurate bound to the burst sources population study in the Schenberg band.

The Ring-Down waveform was used to study the f-mode signatures on the LIGO data, considering that they can be excited by neutron star glitches. Based on a simple Galactic neutron star distribution model, the pulsar glitch activity, and the intrinsic glitch rates, we roughly evaluate the detectability of f-modes. We chose to analyze the f-modes, as they can be the most frequent source of short GW transients in the Schenberg band. However, despite the energy mainly being stored in the fundamental mode among the oscillation modes, they have low energies when related to NS glitches. It is worth mentioning that f-modes can be generated by other processes that oscillate the neutron star, increasing the event rate and emission energy. The eventual observation of f-modes would give valuable hints about the physical conditions of extremely compact matter in neutrons stars and the EoS would be strongly constrained.

We can study the detectability of other GW burst sources with frequencies in the Schenberg band as done with f-modes. In [ARAUJO et al. \(2006\)](#) it was verified the feasibility of detecting black holes massive astrophysical compact halo objects by the Schenberg antenna, which is sensitive to black holes binaries with an individual mass of $0.5M_{\odot}$ just before coalescing (~ 1 ms). Only a few cycles of the final inspiral would be in the frequency band of [3150-3260] Hz, characterizing a short duration transient. The authors estimated the event rate, in events per year, as a function of the strain sensitivity. Therefore, it is possible to estimate the expected event rate for this source from our detection range results.

Finally, we recall the question made on the work introduction: From a scientific point of view, is the reconstruction of the Schenberg antenna at INPE advantageous? We produced a scientific outline to help answer that question from the state-of-art ap-

proach to GW burst detection and a skeptical view about this project. Indeed, this is not an easy question to reply, because reaching the aSchenberg "ultimate" sensitivity requires the research and development of many technologies and techniques. In this sense, assigning it by an incisive outcome is outside the scope of our work. To answer the question through a robust perspective it is necessary to assess the Schenberg detectability potential by looking for other categories of gravitational wave signals in O3 data, such as continuous signals or from compact binary coalescence. We hope that this work has, at least, helped to enlighten this scenario.

REFERENCES

- ABADIE, J. et al. All-sky search for gravitational-wave bursts in the first joint ligo-geo-virgo run. **Physical Review D**, v. 81, p. 102001, May 2010. Available from: <<https://link.aps.org/doi/10.1103/PhysRevD.81.102001>>. 36
- _____. All-sky search for gravitational-wave bursts in the second joint ligo-virgo run. **Physical Review D**, v. 85, p. 122007, Jun 2012. Available from: <<https://link.aps.org/doi/10.1103/PhysRevD.85.122007>>. 36, 57
- ABBOTT, B. et al. Upper limits on gravitational wave bursts in LIGO's second science run. **Physical Review D**, v. 72, n. 6, p. 062001, sep. 2005. 36
- ABBOTT, B. P. et al. Gw150914: First results from the search for binary black hole coalescence with advanced ligo. **Physical Review D**, v. 93, p. 122003, Jun 2016. Available from: <<https://link.aps.org/doi/10.1103/PhysRevD.93.122003>>. 27
- _____. Gw150914: The advanced ligo detectors in the era of first discoveries. **Physical Review Letters**, v. 116, p. 131103, Mar 2016. Available from: <<https://link.aps.org/doi/10.1103/PhysRevLett.116.131103>>. 22
- _____. Observation of gravitational waves from a binary black hole merger. **Physical Review Letters**, v. 116, p. 061102, Feb 2016. Available from: <<https://link.aps.org/doi/10.1103/PhysRevLett.116.061102>>. 1, 14, 15
- _____. All-sky search for short gravitational-wave bursts in the first advanced ligo run. **Physical Review D**, v. 95, n. 4, p. 042003, feb. 2017. 36, 49, 52
- _____. Gw170817: observation of gravitational waves from a binary neutron star inspiral. **Physical Review Letters**, v. 119, p. 161101, Oct 2017. Available from: <<https://link.aps.org/doi/10.1103/PhysRevLett.119.161101>>. 1
- _____. All-sky search for short gravitational-wave bursts in the second advanced ligo and advanced virgo run. **Physical Review D**, v. 100, p. 024017, Jul 2019. Available from: <<https://link.aps.org/doi/10.1103/PhysRevD.100.024017>>. 36, 42, 52
- _____. Gwtc-1: A gravitational-wave transient catalog of compact binary mergers observed by ligo and virgo during the first and second observing runs. **Physical Review X**, v. 9, p. 031040, Sep 2019. Available from: <<https://link.aps.org/doi/10.1103/PhysRevX.9.031040>>. 1, 14

- _____. Properties of the binary neutron star merger GW170817. **Physical Review X**, v. 9, n. 1, p. 011001, jan. 2019. 14
- _____. Search for transient gravitational-wave signals associated with magnetar bursts during advanced ligo's second observing run. **The Astrophysical Journal**, v. 874, n. 2, p. 163, Apr 2019. ISSN 1538-4357. Available from: <<http://dx.doi.org/10.3847/1538-4357/ab0e15>>. 16
- _____. A guide to LIGO–virgo detector noise and extraction of transient gravitational-wave signals. **Classical and Quantum Gravity**, v. 37, n. 5, p. 055002, feb 2020. Available from: <<https://doi.org/10.1088/1361-6382/ab685e>>. 24, 26, 27, 28, 29
- ABBOTT, R. et al. GWTC-2: compact binary coalescences observed by LIGO and Virgo during the first half of the third observing run. **arXiv e-prints**, p. arXiv:2010.14527, oct. 2020. 1, 14, 23
- _____. All-sky search for long-duration gravitational-wave bursts in the third advanced ligo and advanced virgo run. **Physical Review D**, v. 104, p. 102001, Nov 2021. Available from: <<https://link.aps.org/doi/10.1103/PhysRevD.104.102001>>. 39
- _____. All-sky search for short gravitational-wave bursts in the third advanced ligo and advanced virgo run. **Physical Review D**, v. 104, p. 122004, Dec 2021. Available from: <<https://link.aps.org/doi/10.1103/PhysRevD.104.122004>>. 36, 39, 41, 42, 52, 55
- _____. GWTC-2.1: deep extended catalog of compact binary coalescences observed by LIGO and Virgo during the first half of the third observing Run. **arXiv e-prints**, p. arXiv:2108.01045, aug. 2021. 1, 14
- _____. GWTC-3: compact binary coalescences observed by LIGO and Virgo during the second part of the third observing run. **arXiv e-prints**, p. arXiv:2111.03606, nov. 2021. 1, 14
- ACERNESE, F. et al. Advanced virgo: a second-generation interferometric gravitational wave detector. **Classical and Quantum Gravity**, v. 32, n. 2, p. 024001, dec 2014. Available from: <<https://doi.org/10.1088/0264-9381/32/2/024001>>. 22
- AGUIAR, O. D. et al. The Brazilian gravitational wave detector Mario Schenberg: progress and plans. **Classical and Quantum Gravity**, v. 22, n. 10, p.

S209–S214, apr 2005. Available from:

<<https://doi.org/10.1088/0264-9381/22/10/011>>. 20

_____. Status report of the Schenberg gravitational wave antenna. **Journal of Physics: Conference Series**, v. 363, p. 012003, jun 2012. Available from:

<<https://doi.org/10.1088/1742-6596/363/1/012003>>. 21

ANDERSSON, N.; KOKKOTAS, K. D. Towards gravitational wave asteroseismology. **Monthly Notices of the Royal Astronomical Society**, v. 299, n. 4, p. 1059–1068, oct. 1998. 58, 68

ARAUJO, J. C. N. D. et al. Can black hole macho binaries be detected by the brazilian spherical antenna? In: THE TENTH MARCEL GROSSMANN MEETING. **Proceedings...** World Scientific Publishing Company, 2006. Available from: <http://dx.doi.org/10.1142/9789812704030_0251>. 74

ARAUJO, J. C. N. de; MIRANDA, O. D.; AGUIAR, O. D. Detectability of f-mode unstable neutron stars by the Schenberg spherical antenna. **Classical and Quantum Gravity**, v. 22, n. 10, p. S471–S477, may 2005. 67, 72

BAKER, J. et al. The laser interferometer space antenna: unveiling the millihertz gravitational wave sky. **arXiv e-prints**, p. arXiv:1907.06482, jul. 2019. 24

BASU, A. et al. The Jodrell bank glitch catalogue: 106 new rotational glitches in 70 pulsars. **Monthly Notices of the Royal Astronomical Society**, v. 510, n. 3, p. 4049–4062, mar. 2022. 70, 71

BRACEWELL, R. N. **The fourier transform and its applications**. New York: McGraw-Hill, 2000. 24, 42, 62

BRADY, P. R.; CREIGHTON, J. D. E.; WISEMAN, A. G. Upper limits on gravitational-wave signals based on loudest events. **Classical and Quantum Gravity**, v. 21, n. 20, p. S1775–S1781, oct. 2004. 65

CARROLL, S. M. **Lecture notes on general relativity**. [S.l.]: University of Chicago, 1997. 8, 10

CLARK, J. et al. Prospects for high frequency burst searches following binary neutron star coalescence with advanced gravitational wave detectors. **Physical Review D**, v. 90, p. 062004, Sep 2014. Available from:

<<https://link.aps.org/doi/10.1103/PhysRevD.90.062004>>. 58

COSTA, C. A. et al. The Schenberg data acquisition and analysis: results from its first commissioning run. **Classical and Quantum Gravity**, v. 25, n. 18, p. 184002, sep. 2008. 20, 21

CREIGHTON, J. D. E.; ANDERSON, W. G. **Gravitational-wave physics and astronomy: an introduction to theory, experiment and data analysis**. [S.l.: s.n.], 2011. 11, 13, 16, 17

DAVIS, D. **Introduction to searches for gravitational waves with PyCBC**. [S.l.], 2020. Available from: <<https://www.gw-openscience.org/static/workshop3/>>. 43

DAVIS, D. et al. **Data quality vetoes applied to the analysis of LIGO data from the third observing run**. [S.l.], 2021. Available from: <<https://dcc.ligo.org/LIGO-T2100045/public>>. 40

_____. LIGO detector characterization in the second and third observing runs. **Classical and Quantum Gravity**, v. 38, n. 13, p. 135014, jun 2021. Available from: <<https://doi.org/10.1088/1361-6382/abfd85>>. 39, 40

D'INVERNO, R. **Introducing Einstein's relativity**. [S.l.]: Clarendon Press, 1992. 5, 7

DRAGO, M. **Search for transient gravitational wave signals with a known waveform in the LIGO Virgo network of interferometric detectors using a fully coherent algorithm**. Thesis (Ph.D.) — University of Padua, 2010. 36, 65

DRAGO, M. et al. coherent waveburst, a pipeline for unmodeled gravitational-wave data analysis. **SoftwareX**, v. 14, p. 100678, 2021. ISSN 2352-7110. Available from: <<https://www.sciencedirect.com/science/article/pii/S2352711021000236>>. 33, 39

EVANS, M. et al. A horizon study for cosmic explorer: science, observatories, and community. **arXiv e-prints**, p. arXiv:2109.09882, sep. 2021. 24

FELDMAN, G. J.; COUSINS, R. D. Unified approach to the classical statistical analysis of small signals. **Physical Review D**, v. 57, n. 7, p. 3873–3889, apr. 1998. 65

GAYATHRI, V. et al. Astrophysical signal consistency test adapted for gravitational-wave transient searches. **Physical Review D**, v. 100, p. 124022, Dec 2019. Available from: <<https://link.aps.org/doi/10.1103/PhysRevD.100.124022>>. 31

GLAMPEDAKIS, K.; GUALTIERI, L. Gravitational waves from single neutron stars: an advanced detector era survey. In: REZZOLA, L. et al. (Ed.).

Astrophysics and space science library. [S.l.: s.n.], 2018. (Astrophysics and space science library, v. 457), p. 673. 58

HO, W. C. G. et al. Gravitational waves from transient neutron star f-mode oscillations. **Physical Review D**, v. 101, n. 10, p. 103009, may 2020. 67

KEPPEL, D. G. **Signatures and dynamics of compact binary coalescences and a search in LIGO's S5 data**. Thesis (Ph.D.) — California Institute of Technology, Pasadena, 2009. Available from: <https://resolver.caltech.edu/CaltechETD:etd-05202009-115750>. Access in: 2021. 48, 54

KLIMENKO, S.; MITSELMAKHER, G. A wavelet method for detection of gravitational wave bursts. **Classical and Quantum Gravity**, v. 21, n. 20, p. S1819–S1830, sep 2004. Available from: <https://doi.org/10.1088/0264-9381/21/20/025>. 29

KLIMENKO, S. et al. Method for detection and reconstruction of gravitational wave transients with networks of advanced detectors. **Physical Review D**, v. 93, p. 042004, Feb 2016. Available from: <https://link.aps.org/doi/10.1103/PhysRevD.93.042004>. 30, 31

_____. **MDC engine**. Aug 2020. Available from: <https://ldas-jobs.ligo.caltech.edu/~waveburst/waveburst/WWW/doc/cwb/man/mdc.html?highlight=mdc#mdc-engine>. 56

_____. **cWB pipeline library: 6.4.1**. Zenodo, dec. 2021. Available from: <https://doi.org/10.5281/zenodo.5798976>. 38

_____. **coherent WaveBurst**. 2022. Available from: <https://gwburst.gitlab.io/>. 38

KLIS, M. van der. **Fourier techniques in X-ray timing**. Dordrecht: Springer, 1989. 25

LIGO SCIENTIFIC COLLABORATION AND VIRGO COLLABORATION. **O3 data sets**. 2020. Available from: <https://www.gw-openscience.org/O3/>. 40

_____. **Gravitational wave open science center**. 2022. Available from: <https://www.gw-openscience.org/>. 23

- LVK, S. C. **LIGO and Virgo calibration uncertainty (O1, O2 and O3)**. [S.l.], 2021. Available from: <<https://dcc.ligo.org/T2100313/public>>. 40
- MAGGIORE, M. **Gravitational Waves. Vol. 1: Theory and Experiments**. [S.l.]: Oxford University Press, 2007. (Oxford Master Series in Physics). ISBN 978-0-19-857074-5, 978-0-19-852074-0. 2, 7, 9, 12, 19, 24
- MAGGIORE, M. et al. Science case for the Einstein telescope. **Journal of Cosmology and Astroparticle Physics**, v. 2020, n. 3, p. 050, mar. 2020. 24
- MARKOWITZ, J. et al. Gravitational wave burst source direction estimation using time and amplitude information. **Physical Review D**, v. 78, p. 122003, Dec 2008. Available from: <<https://link.aps.org/doi/10.1103/PhysRevD.78.122003>>. 57
- MISNER, C. W.; THORNE, K. S.; WHEELER, J. A. **Gravitation**. San Francisco: W. H. Freeman, 1973. ISBN 978-0-7167-0344-0, 978-0-691-17779-3. 6, 10, 12
- MÉSZÁROS, P. et al. Multi-messenger astrophysics. **Nature Reviews Physics**, v. 1, n. 10, p. 585–599, Oct 2019. ISSN 2522-5820. Available from: <<http://dx.doi.org/10.1038/s42254-019-0101-z>>. 1
- Necula, V.; Klimentko, S.; Mitselmakher, G. Transient analysis with fast Wilson-Daubechies time-frequency transform. In: **Journal of Physics Conference Series**. [S.l.: s.n.], 2012. (Journal of Physics Conference Series, v. 363), p. 012032. 30
- OLIVEIRA, N. F.; AGUIAR, O. D. The Mario Schenberg gravitational wave antenna. **Brazilian Journal of Physics**, v. 46, n. 5, p. 596–603, 2016. 2, 35
- PANKOW, C. et al. Improvements in gravitational-wave sky localization with expanded networks of interferometers. **The Astrophysical Journal**, v. 854, n. 2, p. L25, feb 2018. Available from: <<https://doi.org/10.3847/2041-8213/aaacd4>>. 29
- PAULA, L. A. N. de et al. High-q superconducting niobium cavities for gravitational wave detectors. **Journal of Instrumentation**, v. 9, n. 10, p. P10001–P10001, oct 2014. Available from: <<https://doi.org/10.1088/1748-0221/9/10/p10001>>. 21
- REED, B. T.; DEIBEL, A.; HOROWITZ, C. J. Modeling the galactic neutron star population for use in continuous gravitational-wave searches. **The Astrophysical**

Journal, v. 921, n. 1, p. 89, nov 2021. Available from:
<<https://doi.org/10.3847/1538-4357/ac1c04>>. 68, 71

REIS, A. P. **Improving the calculation of the sensitivity curve and frequency arrangement of the Schenberg GW detector**. 69 p. Dissertation (Master in Astrophysics) — Instituto Nacional de Pesquisas Espaciais (INPE), São José dos Campos, 2021. Available from:
<<http://mtc-m21d.sid.inpe.br/ibi/8JMKD3MGP3W34T/44TS9CL>>. 35

RILES, K. Recent searches for continuous gravitational waves. **Modern Physics Letters A**, v. 32, n. 39, p. 1730035–685, dec. 2017. 16

SATHYAPRAKASH, B. S.; SCHUTZ, B. F. Physics, astrophysics and cosmology with gravitational waves. **Living Reviews in Relativity**, v. 12, n. 1, Mar 2009. ISSN 1433-8351. Available from: <<http://dx.doi.org/10.12942/lrr-2009-2>>. 12, 14

SCHUTZ, B. F. Networks of gravitational wave detectors and three figures of merit. **Classical and Quantum Gravity**, v. 28, n. 12, p. 125023, may 2011. Available from: <<https://doi.org/10.1088/0264-9381/28/12/125023>>. 28

SUN, L. et al. Characterization of systematic error in advanced LIGO calibration. **Classical and Quantum Gravity**, v. 37, n. 22, p. 225008, oct 2020. Available from: <<https://doi.org/10.1088/1361-6382/abb14e>>. 40, 41

_____. Characterization of systematic error in Advanced LIGO calibration in the second half of O3. **arXiv e-prints**, p. arXiv:2107.00129, jun. 2021. 40

SUTTON, P. J. Upper limits from counting experiments with multiple pipelines. **Classical and Quantum Gravity**, v. 26, n. 24, p. 245007, dec. 2009. 65

_____. A rule of thumb for the detectability of gravitational-wave bursts. **arXiv e-prints**, p. arXiv:1304.0210, mar. 2013. 62

TIEC, A. L.; NOVAK, J. Theory of gravitational waves. **An Overview of Gravitational Waves**, p. 1–41, Feb 2017. Available from:
<http://dx.doi.org/10.1142/9789813141766_0001>. 11

WAŚ, M. et al. On the background estimation by time slides in a network of gravitational wave detectors. **Classical and Quantum Gravity**, v. 27, n. 1, p. 015005, jan. 2010. 42

WHEELER, J. A.; FORD, K. **Geons, black holes, and quantum foam: a life in physics.** [S.l.: s.n.], 1998. 6

YUSIFOV, I.; KÜÇÜK, I. Revisiting the radial distribution of pulsars in the galaxy. **Astronomy & Astrophysics (A&A)**, v. 422, n. 2, p. 545–553, 2004. Available from: <<https://doi.org/10.1051/0004-6361:20040152>>. 71

ZHENG, Y. et al. A needle in (many) haystacks: using the false alarm rate to sift gravitational waves from noise. **Significance**, v. 18, p. 26–31, 02 2021. 56

APÊNDICE A

A.1 Detection parameters of zero-lag triggers

In this section the detection parameters of candidate events to GW burst signals from our search results, separated into the respective chunks are presented. Let us recall that all zero-lag triggers had the same significance distribution for the expected background.

Table A.1 - Significance parameters of zero-lag triggers of chunk 1.

Run	Chunk	GPS time	IFAR (years)	livetime (years)	Expected #	Observed #	FAP
O3a	1	1241100945.3837	0.132	0.0593891	0.450	1	0.362
O3a	1	1239216680.8997	0.020	0.0593891	2.969	2	0.949
O3a	1	1241101731.1742	0.013	0.0593891	4.441	3	0.988
O3a	1	1239683368.6574	0.011	0.0593891	5.376	4	0.995
O3a	1	1239026974.9329	0.010	0.0593891	5.791	5	0.997
O3a	1	1238851028.5194	0.009	0.0593891	6.380	6	0.998
O3a	1	1238655419.4109	0.008	0.0593891	7.038	7	0.999
O3a	1	1239798593.2831	0.008	0.0593891	7.237	8	0.999
O3a	1	1240055172.5791	0.006	0.0593891	9.617	9	≈ 1.000
O3a	1	1241808485.1350	0.006	0.0593891	10.091	10	≈ 1.000
O3a	1	1238401570.3509	0.005	0.0593891	11.793	11	≈ 1.000

Table A.2 - Significance parameters of zero-lag triggers of chunk 2.

Run	Chunk	GPS time	IFAR (years)	livetime (years)	Expected #	Observed #	FAP
O3a	2	1244599768.0025	0.558	0.2214161	0.397	1	0.328
O3a	2	1248701512.4219	0.081	0.2214161	2.730	2	0.935
O3a	2	1242819814.5325	0.080	0.2214161	2.767	3	0.937
O3a	2	1253805507.1575	0.049	0.2214161	4.474	4	0.989
O3a	2	1244147273.1322	0.040	0.2214161	5.481	5	0.996

Table A.3 - Significance parameters of zero-lag triggers of chunk 3.

Run	Chunk	GPS time	IFAR (years)	livetime (years)	Expected #	Observed #	FAP
O3b	3	1267737402.7162	0.249	0.255863	1.027	1	0.642
O3b	3	1268981400.9633	0.145	0.255863	1.759	2	0.828
O3b	3	1266374948.0090	0.113	0.255863	2.263	3	0.896
O3b	3	1258372645.5377	0.111	0.255863	2.301	4	0.900
O3b	3	1258060361.2617	0.096	0.255863	2.657	5	0.930
O3b	3	1257856381.0558	0.070	0.255863	3.676	6	0.975
O3b	3	1261333608.1994	0.068	0.255863	3.766	7	0.977
O3b	3	1258013262.2466	0.051	0.255863	4.978	8	0.993
O3b	3	1257771667.8899	0.050	0.255863	5.128	9	0.994
O3b	3	1257658584.5580	0.047	0.255863	5.399	10	0.995
O3b	3	1257667131.3351	0.046	0.255863	5.582	11	0.996
O3b	3	1258865493.8634	0.043	0.255863	5.980	12	0.997
O3b	3	1257780090.9774	0.042	0.255863	6.139	13	0.998
O3b	3	1258288176.5319	0.039	0.255863	6.636	14	0.999
O3b	3	1258972087.7265	0.027	0.255863	9.523	15	≈ 1.000
O3b	3	1264829332.7924	0.026	0.255863	9.692	16	≈ 1.000
O3b	3	1260159761.1127	0.024	0.255863	10.451	17	≈ 1.000
O3b	3	1258257271.4011	0.024	0.255863	10.466	18	≈ 1.000
O3b	3	1258716489.5189	0.022	0.255863	11.803	19	≈ 1.000
O3b	3	1267983992.1732	0.020	0.255863	13.011	20	≈ 1.000
O3b	3	1258684358.9902	0.019	0.255863	13.169	21	≈ 1.000
O3b	3	1267747805.6071	0.019	0.255863	13.575	22	≈ 1.000
O3b	3	1260521223.5616	0.017	0.255863	14.689	23	≈ 1.000
O3b	3	1257674960.2075	0.017	0.255863	15.339	24	≈ 1.000
O3b	3	1264825714.6949	0.015	0.255863	16.774	25	≈ 1.000